LITHOS

EoS of mantle minerals coupled with composition and thermal state of the lithosphere: inferring the density structure of peridotitic systems

--Manuscript Draft--

Manuscript Number:	LITHOS9759R2
Article Type:	Regular Article
Keywords:	Equations of State, Mantle minerals, Upper mantle density structure, Fertile and depleted peridotites, Cold-hot geotherms
Corresponding Author:	Luca Faccincani, M.D. University of Ferrara Department of Physics and Earth Sciences: Universita degli Studi di Ferrara Dipartimento di Fisica e Scienze della Terra Ferrara, Ferrara ITALY
First Author:	Luca Faccincani, M.D.
Order of Authors:	Luca Faccincani, M.D.
	Barbara Faccini
	Federico Casetta
	Maurizio Mazzucchelli
	Fabrizio Nestola
	Massimo Coltorti
Abstract:	Unravelling the physical state and properties of mantle rocks is crucial for understanding both plate tectonics, seismic activity, and volcanism. In this context, the knowledge of accurate elastic parameters of constituent mineral phases, and their variations with pressure (P) and temperature (T), is an essential requirement, that coupled with the thermal state of the lithosphere can provide a better understanding of its petrophysics and thermochemical structure. In this paper, we present an assessment of the thermoelastic parameters [in the form of P–V–T–K Equations of State (EoS)] of orthopyroxene, clinopyroxene, spinel and garnet based on X-Ray diffraction data and direct elastic measurements available in literature. The newly developed EoS are appropriate to describe the elastic behaviour of these phases under the most relevant P–T conditions and bulk compositions of the Earth's mantle. In combination with the published EoS for mantle olivine and magnesiochromite, these EoS are suitable to calculate the physical properties of mantle peridotites and their variation with P and T. Thanks to these EoS, we can evaluate how the variations in bulk composition and thermal regimes affect the density structure of the lithospheric mantle. Accordingly, the density structure of fertile and depleted peridotitic systems was calculated along the 35, 45 and 60 mWm -2 geothermal gradients at P comprised between 1 and 8 GPa. Under very cold geothermal gradients, the density of both fertile and depleted peridotitic systems progressively increases with depth, whereas under relatively hot conditions a first downwards decrease from 1 to ca 3 GPa is observed, followed by an increase downward. In mantle sections characterized by intermediate geotherms (45 mWm -2), the behaviour of the two systems differs up to ca 4 GPa, as the density of the depleted system remains nearly constant down to this depth whereas it moderately increases in the fertile system. The results of our simplified parameterisation, in agreement with classical thermodynamic modelling, indicate that the density structure of the lithospheric mantle is predominantly controlled by the P – T gradient variations, with some compositional control mostly arising at cold-intermediate thermal conditions. Integrated by geophysical and thermodynamic modelling, the newly developed and selected EoS could provide an alternative strategy to infer the elastic properties of mineral phases and peridotite rocks, under the most relevant P–T conditions and compositions of the Earth's mantle, without requiring sets of end-member properties and solution models.

Suggested Reviewers:	Luca Ziberna luca.ziberna@units.it
	Michel Grégoire michel.gregoire@get.omp.eu
	Razvan Caracas razvan.caracas@ens-lyon.fr
	Günther Redhammer guenther.redhammer@sbg.ac.at
	Joseph R. Smyth joseph.smyth@colorado.edu
	Tiziana Boffa Ballaran tiziana.boffa-ballaran@uni-bayreuth.de
Opposed Reviewers:	

EoS of mantle minerals coupled with composition and thermal state of the lithosphere: inferring the density structure of peridotitic systems

Luca Faccincani[1,*], Barbara Faccini[1], Federico Casetta[1,2], Maurizio Mazzucchelli[3], Fabrizio Nestola[4] and Massimo Coltorti[1,5]

[1] *Department of Physics and Earth Sciences, University of Ferrara, Via Saragat 1, 44121 Ferrara, Italy*

[2] *Department of Lithospheric Research, University of Vienna, Althanstraße 14, 1090 Vienna, Austria*

[3] *Department of Chemical and Geological Sciences, University of Modena and Reggio Emilia, Via Campi 103, 41125 Modena, Italy*

[4] *Department of Geosciences, University of Padua, Via Gradenigo 6, 35131 Padua, Italy*

[5] *Istituto Nazionale di Geofisica e Vulcanologia (INGV) Sezione di Palermo, Via Ugo la Malfa 153, 90146 Palermo, Italy*

*** Corresponding author:** Luca Faccincani; email: luca.faccincani@unife.it

UNIVERSITA' DEGLI STUDI DI FERRARA
DEPARTMENT OF PHYSICS AND EARTH SCIENCES
Via Giuseppe Saragat, 1 - 44122 FERRARA (Italy)
Phone: +39-0532974671

Ferrara, August 8th, 2021

To the Editors of *Lithos*

Dear Editor,

Please find enclosed the revised version of the manuscript, re-titled **"EoS of mantle minerals coupled with composition and thermal state of the lithosphere: inferring the density structure of peridotitic systems"** by Luca Faccincani, Barbara Faccini, Federico Casetta, Maurizio Mazzucchelli, Fabrizio Nestola and Massimo Coltorti for publication in *Lithos*.

This manuscript presents the results of an integrated study of the density structure of the lithospheric mantle based on mineral physics and petrological data of the constituent minerals of mantle peridotites. The assessment of the thermoelastic parameters of mantle minerals, in terms of their Equations of State, was coupled with petrological features to investigate the density structure of fertile and depleted peridotitic systems under different thermal regimes and bulk compositions.

The results showed that the density structure of the lithospheric mantle is predominantly controlled by the thermal state and only marginally by the mineralogical composition of mantle peridotites. Indeed, the density evolution with depth of both fertile and depleted peridotitic systems exhibits similar trends under very cold (35 mWm^{-2}) and relatively hot (60 mWm^{-2}) conditions and only differs under intermediate (45 mWm^{-2}) conditions.

In the existing literature, density models of the upper mantle are predominantly extrapolated from computations of equilibrium assemblages and phase relations at specific P – T – X conditions. In our study, we showed that density profiles in natural systems can be computed with enough accuracy also with simplified phase relations. This is further supported by the application of our model in comparison with classic thermodynamic modelling (Perple_X) results from literature.

The novelty and main results of this manuscript are significant to a better understanding of the density structure of the lithospheric mantle under different compositions and thermal regimes. We also believe that the integration of our data in geophysical and thermodynamic modelling could provide independent constraints on the behaviour of peridotitic systems in the lithosphere and therefore could help in better assessing its thermochemical structure.

This manuscript is an original work and has not been previously published or been under consideration for publication elsewhere. All authors believe that this manuscript could be of great interest for the scientific community and agree on the submission to *Lithos*.

Taking into account the scientific context of this study, numerous colleagues would provide very useful contribution to improve this work, the following being especially helpful:

1. Dr. Luca Ziberna

Department of Mathematics and Geoscience
University of Trieste
Via Weiss 2, 34128 Trieste, Italy
Email: luca.ziberna@units.it

2. Dr. Michel Grégoire
Géosciences Environnement Toulouse, Observatoire Midi-Pyrénées
14 Avenue E. Belin, 31400 Toulouse, France
Email: michel.gregoire@get.omp.eu

3. Prof. Razvan Caracas
CNRS, Ecole Normale Supérieure de Lyon,
Laboratoire de Géologie de Lyon UMR 5276, Centre Blaise Pascal,
46 allée d'Italie, 69364 Lyon, France
Email: razvan.caracas@ens-lyon.fr

4. Prof. Günther Redhammer
Department of Chemistry and Physics of Materials
Division of Materials Science and Mineralogy
University of Salzburg
Jakob-Haringerstr. 2A, 5020 Salzburg, Austria
Email: guenther.redhammer@sbg.ac.at

5. Prof. Joseph R. Smyth
Department of Geological Sciences
University of Colorado
Boulder, CO 80309, USA
Email: joseph.smyth@colorado.edu

6. Dr. Tiziana Boffa Ballaran
Bayerisches Geoinstitut
Universität Bayreuth
95440 Bayreuth, Germany
Email: tiziana.boffa-ballaran@uni-bayreuth.de

Thank you very much for your consideration and handling.

On behalf of co-authors,

Luca Faccincani

To the Editor of *Lithos*

Dear Editor,

Please find enclosed the final revised version of the manuscript, titled **"EoS of mantle minerals coupled with composition and thermal state of the lithosphere: inferring the density structure of peridotitic systems"** by Luca Faccincani, Barbara Faccini, Federico Casetta, Maurizio Mazzucchelli, Fabrizio Nestola and Massimo Coltorti for publication in *Lithos*.

We took into account Reviewer's #1 proposed corrections, and accomplished all of them. You will find our revised work in the docx file "Faccincani et al., manuscript_Changes marked", which includes the (very few) new parts with red typing. Clean version (black typing) of the revised manuscript is also provided ("Faccincani et al., Manuscript").

Thank you very much for your consideration and handling.

On behalf of co-authors,

Luca Faccincani

Luca Faccincani, Ph.D. student. Department of Physics and Earth Sciences, University of Ferrara, Via Saragat 1, 44121 Ferrara, Italy. Email: luca.faccincani@unife.it

Abstract

Unravelling the physical state and properties of mantle rocks is crucial for understanding both plate tectonics, seismic activity, and volcanism. In this context, the knowledge of accurate elastic parameters of constituent mineral phases, and their variations with pressure (P) and temperature (T), is an essential requirement, that coupled with the thermal state of the lithosphere can provide a better understanding of its petrophysics and thermochemical structure.

In this paper, we present an assessment of the thermoelastic parameters [in the form of P–V–T–K Equations of State (EoS)] of orthopyroxene, clinopyroxene, spinel and garnet based on X-Ray diffraction data and direct elastic measurements available in literature. The newly developed EoS are appropriate to describe the elastic behaviour of these phases under the most relevant P–T conditions and bulk compositions of the Earth's mantle. In combination with the published EoS for mantle olivine and magnesiochromite, these EoS are suitable to calculate the physical properties of mantle peridotites and their variation with P and T.

Thanks to these EoS, we can evaluate how the variations in bulk composition and thermal regimes affect the density structure of the lithospheric mantle. Accordingly, the density structure of fertile and depleted peridotitic systems was calculated along the 35, 45 and 60 mWm^{-2} geothermal gradients at P comprised between 1 and 8 GPa. Under very cold geothermal gradients, the density of both fertile and depleted peridotitic systems progressively increases with depth, whereas under relatively hot conditions a first downwards decrease from 1 to ca 3 GPa is observed, followed by an increase downward. In mantle sections characterized by intermediate geotherms (45 mWm^{-2}), the behaviour of the two systems differs up to ca 4 GPa, as the density of the depleted system remains nearly constant down to this depth whereas it moderately increases in the fertile system.

The results of our simplified parameterisation, in agreement with classical thermodynamic modelling, indicate that the density structure of the lithospheric mantle is predominantly controlled by the P – T gradient variations, with some compositional control mostly arising at cold-intermediate thermal conditions. Integrated by geophysical and thermodynamic modelling, the newly developed and selected EoS could provide an alternative strategy to infer the elastic properties of mineral phases and peridotite rocks, under the most relevant P–T conditions and compositions of the Earth's mantle, without requiring sets of end-member properties and solution models.

Keywords: Equations of State, Mantle minerals, Upper mantle density structure, Fertile and depleted peridotites, Cold-hot geotherms

Highlights

- Thermoelastic parameters of mantle peridotite minerals are constrained
- Peridotite density is evaluated under different thermal regimes and compositions
- Thermal state largely controls lithospheric mantle density structure
- High heat flows lead to overall density decrease in the uppermost mantle section
- Low heat flows lead to overall density increase in the entire mantle section

EoS of mantle minerals coupled with composition and thermal state of the lithosphere: inferring the density structure of peridotitic systems

Luca Faccincani[1,*], Barbara Faccini[1], Federico Casetta[1,2], Maurizio Mazzucchelli[3], Fabrizio Nestola[4] and Massimo Coltorti[1,5]

[1] *Department of Physics and Earth Sciences, University of Ferrara, Via Saragat 1, 44121 Ferrara, Italy*

[2] *Department of Lithospheric Research, University of Vienna, Althanstraße 14, 1090 Vienna, Austria*

[3] *Department of Chemical and Geological Sciences, University of Modena and Reggio Emilia, Via Campi 103, 41125 Modena, Italy*

[4] *Department of Geosciences, University of Padua, Via Gradenigo 6, 35131 Padua, Italy*

[5] *Istituto Nazionale di Geofisica e Vulcanologia (INGV) Sezione di Palermo, Via Ugo la Malfa 153, 90146 Palermo, Italy*

*** Corresponding author:** Luca Faccincani; email: luca.faccincani@unife.it

Abstract

Unravelling the physical state and properties of mantle rocks is crucial for understanding both plate tectonics, seismic activity, and volcanism. In this context, the knowledge of accurate elastic parameters of constituent mineral phases, and their variations with pressure (P) and temperature (T), is an essential requirement, that coupled with the thermal state of the lithosphere can provide a better understanding of its petrophysics and thermochemical structure.

In this paper, we present an assessment of the thermoelastic parameters [in the form of P–V–T–K Equations of State (EoS)] of orthopyroxene, clinopyroxene, spinel and garnet based on X-Ray diffraction data and direct elastic measurements available in literature. The newly developed EoS are appropriate to describe the elastic behaviour of these phases under the most relevant P–T conditions and bulk compositions of the Earth's mantle. In combination with the published EoS for mantle olivine and magnesiochromite, these EoS are suitable to calculate the physical properties of mantle peridotites and their variation with P and T.

Thanks to these EoS, we can evaluate how the variations in bulk composition and thermal regimes affect the density structure of the lithospheric mantle. Accordingly, the density structure of fertile and depleted peridotitic systems was calculated along the 35, 45 and 60 mWm^{-2} geothermal gradients at P comprised between 1 and 8 GPa. Under very cold geothermal gradients, the density of both fertile and depleted peridotitic systems progressively increases with depth, whereas under relatively hot conditions a first downwards decrease from 1 to ca 3 GPa is observed, followed by an increase downward. In mantle sections characterized by intermediate geotherms (45 mWm^{-2}), the behaviour of the two systems differs up to ca 4 GPa, as the density of the depleted system remains nearly constant down to this depth whereas it moderately increases in the fertile system.

The results of our simplified parameterisation, in agreement with classical thermodynamic modelling, indicate that the density structure of the lithospheric mantle is predominantly controlled by the P – T gradient variations, with some compositional control mostly arising at cold-intermediate thermal conditions. Integrated by geophysical and thermodynamic modelling, the newly developed and selected EoS could provide an alternative strategy to infer the elastic properties of mineral phases and peridotite rocks, under the most relevant P–T conditions and compositions of the Earth's mantle, without requiring sets of end-member properties and solution models.

Keywords: Equations of State, Mantle minerals, Upper mantle density structure, Fertile and depleted peridotites, Cold-hot geotherms

1. Introduction

Understanding the density structure of the upper mantle is critical to our comprehension of the tectonic and magmatic evolution of the lithosphere (e.g., Braun, 2010; Capitanio et al., 2007; Simon and Podladchikov, 2008; Thybo and Artemieva, 2013) and crucial to address complex geodynamic phaenomena (e.g., mantle convection, plume upwelling, slab subduction, crustal movements). The density of the upper mantle ultimately depends on both its thermal and compositional structure, which

55 can be derived from petrological-geochemical studies on exhumed mantle samples, i.e., xenoliths and
56 tectonically exposed mantle sections, and from the interpretation of seismic data (and in general of
57 geophysical observables, e.g., gravity anomalies, surface heat flow, etc.).
58 Thermobarometric, petrochemical and isotopic studies of xenoliths and exposed mantle sections can
59 help in unveiling the compositional and thermal structure of their source mantle at the time of the
60 eruption or emplacement (e.g., Coltorti et al., 2021; Mazzucchelli et al., 2009; Melchiorre et al., 2020;
61 Pearson et al., 2003) but the structure of the lithosphere may only be defined at a local scale, as large
62 portions remain inaccessible. Differently, seismic data are endowed with a more continuous spatial
63 coverage, to such an extent that the mantle may be imaged at a lithospheric scale; however, their
64 conversion into models of the upper mantle is not straightforward (Afonso et al., 2013, and references
65 therein). The interpretation of seismic data relies on appropriate combinations of the observed seismic
66 wave velocities with either thermodynamic concepts and/or experimental data from mineral physics
67 (e.g., Bass and Anderson, 1984) and needs to account for both compositional and thermal signatures
68 in wave velocities. Uncertainties in data interpretation are further exacerbated since ultramafic rocks
69 with different compositions can fit equally well wave velocities (e.g., Afonso et al., 2013).
70 In general, addressing the thermochemical structure of the mantle requires the calculation of mineral
71 and rock physical properties (elastic *moduli*, thermal expansions, densities, etc.) at elevated pressure
72 and temperature. Unequivocally, the knowledge of accurate elastic parameters of candidate mantle
73 phases, and their variations with pressure and temperature, is required. In this context, the Equations
74 of State (EoS) of mantle phases are undoubtedly the best proxy for unravelling the structure and
75 dynamics of the Earth's mantle (e.g., Afonso et al., 2007; Stixrude and Lithgow-Bertelloni, 2005a)
76 and its evolution through time, as they can define how volume, density or the elastic properties of
77 minerals vary with pressure and/or temperature (e.g., Angel, 2000). For rocks, the elastic properties
78 have to be inferred from those of their constituent minerals, at appropriate conditions (Connolly,
79 2009). This is commonly done by phase equilibria calculations based on thermodynamic data (Afonso
80 et al., 2008; Connolly and Petrini, 2002; Stixrude and Lithgow-Bertelloni, 2011, 2005b) (see

Connolly, 2009 for extensive considerations of phase equilibria calculations to geodynamic modelling), with aggregate properties calculated by any standard solid mixing theory (e.g., Abers and Hacker, 2016; Hacker and Abers, 2004, and references therein). As mass in aggregates is a simple sum of chemical component masses, the density of rocks can be then calculated from the density of constituent minerals according to their volume proportion.

Several studies attempted to evaluate the density distribution of the lithosphere, known to be vertically and laterally heterogeneous due to variable mineralogy (in terms of mineral and modal compositions), complex phase transitions and differing thermal regimes. It was showed that the increase of Mg/(Mg+Fe) during partial melting lowers the bulk density of the mantle (Schutt and Lesher 2006), but is not affecting phase transitions unlike Na content, which controls the spinel – plagioclase transition and may play an important role in areas of high heat flows and thin crust (Simon and Podladchikov, 2008). Further studies investigated the density structure of mantle sections either by combining data from petrology, mineral physics and geophysics (e.g., Fullea et al., 2014) or by classic thermodynamic calculations complemented for the most relevant Cr-bearing phases in the upper mantle (Ziberna and Klemme, 2016). These studies showed some contrasting results as to whether the predominant control on the density variations of the lithosphere is due to the thermal state, bulk composition, or their interplay.

In this work, we set out to explore the density structure of the lithospheric mantle, and its variation with changes in bulk composition and thermal gradient, from the perspective of the EoS of its constituent minerals, following a simplified parameterisation. The first part presents an assessment of the thermoelastic parameters of orthopyroxene, clinopyroxene, spinel and garnet. To this aim, pre-existing literature data on compressibility, thermal expansion and elasticity of these phases were used to constrain their P–V–T–K (P = pressure, V = volume, T = temperature, K = bulk modulus) EoS in peridotitic systems (i.e., preferentially selecting data measured on crystals with chemical compositions comparable to those expected in the upper mantle). As already computed in recent detailed studies, P–V–T–K and P–V–T EoS for mantle olivine and magnesiochromite were selected

from literature (Angel et al., 2018; Nestola et al., 2019); two distinct EoS were used for mantle spinels to account for the variation of their elastic properties in response to varying Cr and Al contents (cfr. Section 2.3). The second part of this work aims at investigating how the density structure of fertile and depleted lithospheric mantle sections is affected by different thermal regimes (35, 45 and 60 mWm^{-2} geothermal gradients), following a simplified parameterisation that does not incorporate phase relations. Beyond exploring the density variations with this approach, we also provide a comparison with classic thermodynamic modelling (Perple_X; Ziberna and Klemme, 2016). This comparison allowed to assess that (i) the density profiles can be readily computed following our simplified parameterisation, (ii) the thermal gradient is the controlling variable when it comes to the density structure of the lithosphere and (iii) the newly developed and selected EoS consistently describe the elastic behaviour of the related phases under the most relevant P–T conditions and compositions of the Earth's mantle, without requiring sets of end-member properties and solution models.

2. Data selection and EoS fitting

There are two possible approaches to describe the P–V–T or P–V–T–K behaviour of solids: thermal-pressure models (Holland-Powell and Mie-Grüneisen-Debye thermal‑pressure EoS) and isothermal-type models at high temperature (cfr. Angel et al., 2018). For extensive considerations to these issues the reader is referred to Anderson (1995), Angel (2000) and Angel et al. (2018).

The thermoelastic properties for mantle olivine (Fo_{90-92}) have been extensively reviewed and the P–V–T–K EoS was recently published (Angel et al., 2018). Considering the P – T ranges of our investigation, we selected the third-order Birch-Murnaghan compressional EoS in combination with the isothermal-type model for all the computations.

The P–V–T EoS for mantle magnesiochromite was also recently published (Nestola et al., 2019), parametrised as second-order Birch-Murnaghan compressional EoS in combination with the Holland-Powell thermal‑pressure EoS; this formulation was used for the computations of magnesiochromite

for the depleted peridotitic system. The selected thermoelastic parameters for mantle olivine and mantle magnesiochromite are reported in Table 1.

The thermoelastic behaviour of pyroxenes, spinel and garnet was here constrained based on X-Ray diffraction data (compressibility and thermal expansion) and elasticity measurements available in literature. The full EoS for these phases were solved with the EosFit7c program (Angel et al., 2014) following the approach of Milani et al. (2017) to perform simultaneous fits of elastic moduli and cell parameters. For every phase, each individual data set of volumes was scaled to its own volume at room conditions prior to fitting the data together. Additionally, in order to compare X-Ray diffraction and elasticity measurements, K_{SR} (adiabatic Reuss bulk moduli, from elasticity data) were converted into K_{TR} (isothermal Reuss bulk moduli, from X-Ray diffraction data) according to the relationship $K_{SR} = (1 + \alpha_V \gamma T) K_{TR}$ where α_V is the volume thermal expansion (taken from the EoS itself, at the P – T of interest) and γ is the Grüneisen parameter (taken from literature).

2.1 Orthopyroxene

Mantle orthopyroxenes (space group *Pbca*) are solid solutions between enstatite ($Mg_2Si_2O_6$) and ferrosilite ($Fe_2Si_2O_6$) end-members and typically contain few wt% of Al_2O_3 and some CaO as well (e.g., McDonough and Rudnick, 1998). A reanalysis of K_{TR} and its pressure derivative K'_{TR} of $Mg_2Si_2O_6$ based on different experiments (two compression, one Brillouin measurement and one ultrasonic measurement) (Angel and Jackson, 2002) yielded the best estimates of $K_{TR,0}$ and $K'_{TR,0}$, being respectively 105.8(5) GPa and 8.5(3). By comparison, measurements on aluminium-bearing natural orthopyroxenes showed higher bulk moduli and lower pressure derivatives (Chai et al., 1997; Hugh-Jones et al., 1997; Zhang and Bass, 2016, refit of their data) than that of $Mg_2Si_2O_6$. For these reasons, $Mg_2Si_2O_6$ enstatite cannot be considered a good representation of the elastic behaviour of the orthopyroxene component in the lithospheric upper mantle.

We selected data from five different experiments on mantle orthopyroxenes: two compressions (Hugh-Jones and Angel, 1997) [samples *N1* and *N2*]), two expansions (Yang and Ghose, 1994

158 [sample *Fs20*]; Scandolo et al., 2015 [sample *B22 N.60*]) and one high-pressure Brillouin
159 measurement (Zhang and Bass, 2016). We are not aware of any volume measurements on either
160 mantle-composition orthopyroxene or enstatite made at low temperature; consequently, the Einstein
161 temperature (θ_E) could not be refined and was fixed at 510 K (Holland and Powell, 2011,
162 corresponding to Fs20). The Grüneisen parameter (0.85, for Fs20) was taken from Yang and Ghose
163 (1994) and assumed that it does not vary with temperature. With these constraints, we fitted
164 simultaneously each individual data set with a third-order Birch-Murnaghan compressional EoS in
165 combination with the isothermal-type model (parameterisation from Angel et al., 2018); the final
166 refined EoS parameters (Table 1) fit all the data within the experimental uncertainties (Supplementary
167 Material File 1, Figure S1). The final EoS for mantle orthopyroxene is provided in Supplementary
168 Material File 2.
169
170 **2.2 Clinopyroxene**
171 Mantle clinopyroxenes (space group *C2/c*) are solid solutions between diopside ($CaMgSi_2O_6$) and
172 hedenbergite ($CaFeSi_2O_6$) end-members and typically contain few wt% of Al_2O_3, some Cr_2O_3 as well
173 as Na_2O (e.g., McDonough and Rudnick, 1998).
174 A survey of the literature showed that $K_{TR,0}$ and $K'_{TR,0}$ values for $CaMgSi_2O_6$ diopside and near end-
175 member compositions exhibit large variations; the same is for $K_{S,0}$ and $K'_{S,0}$ (see Xu et al., 2019 for a
176 recent compilation of literature data).
177 We selected data from six different experiments on diopside and near end-member compositions: one
178 compression (Li and Neuville, 2010 [room temperature data]), three expansions (Cameron et al., 1973
179 [sample *Diopside*]; Pandolfo et al., 2015 [sample *Di*]; Prencipe et al., 2000), one high-pressure
180 Brillouin measurement (Sang and Bass, 2014) and one high-temperature RUS measurement (Isaak et
181 al., 2006). The Grüneisen parameter (0.867) is taken from Isaak et al. (2006) and assumed that it does
182 not vary with temperature. $K_{SR,0}$ for near end-member diopsides recalculated from C_{ij} data of Sang
183 and Bass (2014) and Isaak et al. (2006) are significantly different between each other (respectively,

111.2(7) GPa vs 113.4(9) GPa). To make the fit consistent between these two data sets, we excluded $K_{SR,0}$ of Sang and Bass (2014). We also excluded from the fit the data point of Sang and Bass (2014) at 14 GPa, which lies completely outside the trend (Supplementary Material File 1, Figure S2). With these constraints, we fitted simultaneously each individual data set with a third-order Birch-Murnaghan compressional EoS in combination with the isothermal-type model (parameterisation from Angel et al., 2018); the final refined EoS parameters (Table 1) fit almost all the data within the experimental uncertainties (Supplementary Material File 1, Figure S2). The final EoS for mantle clinopyroxene is provided in Supplementary Material File 3.

Bearing in mind that the selected data sets correspond to near end-member and $CaMgSi_2O_6$ diopside, it must be considered carefully whether the final refined thermoelastic parameters are a good representation of the elastic behaviour of the clinopyroxene component in the lithospheric upper mantle. Indeed, clinopyroxenes with augitic compositions are a common species occurring in a wide variety of igneous rocks and can be occasionally found in ultrabasic rocks. Xu et al. (2017) and (2019) recently studied the thermoelastic behaviour of augite by synchrotron-based X-Ray diffraction combined with an externally heated diamond anvil cell. Their experiments yielded respectively $K_{TR,0}$ = 111(1) GPa, $K'_{TR,0}$ = 4.1(1) and $K_{TR,0}$ = 112(3) GPa, $K'_{TR,0}$ = 5.0(7). These results prove that clinopyroxenes with augitic compositions behave similarly to near end-member diopsides. Therefore, we are confident that our P–V–T–K EoS parameters can be applied to a wide range of mantle clinopyroxene compositions.

2.3 Spinel

Mantle spinels (space group *Fd-3m*) show extensive solid solution between end-members as they typically vary in composition between four components: spinel s.s. ($MgAl_2O_4$), hercynite ($FeAl_2O_4$), magnesiochromite ($MgCr_2O_4$) and chromite ($FeCr_2O_4$). The compositional variations in mantle spinels are mainly displayed in their Cr/(Cr + Al) and Mg/(Mg + Fe) molar ratios, which reflect the degree of melt depletion experienced by a peridotite. Indeed, spinels with high Al and low Cr contents

characterize lherzolites, whereas low Al and high Cr contents distinguish harzburgitic spinels (e.g., McDonough and Rudnick, 1998).

The bulk modulus systematics for Mg-Fe-Cr-Al spinels have been recently analysed by Nestola et al. (2015, and references therein), who showed that: (i) the Cr-Al substitution considerably changes the $K_{TR,0}$ [192(1) vs 182.5(1.4) GPa for $MgAl_2O_4$ and $MgCr_2O_4$, respectively]; (ii) the Fe-Mg substitution does not substantially affect the bulk modulus for either Cr or Al spinels [193.9(1.7) vs 184.8(1.7) GPa for $FeAl_2O_4$ and $FeCr_2O_4$, respectively], with the $K'_{TR,0}$ similar for all four end-members. Thus, the $K_{TR,0}$ of Mg-Fe-Cr-Al spinels is roughly controlled by the Cr/Al ratio. Hence, two EoS are needed to properly describe the elastic behaviour of mantle spinels: one EoS for lherzolitic spinels and another EoS (selected from Nestola et al., 2019, see above) for harzburgitic spinels (magnesiochromites).

To constrain the elastic behaviour of Al-rich lherzolitic spinels, we selected data from six different experiments: one compression (Nestola et al., 2007 [sample *disordered*]), three expansions (Carbonin et al., 2002 [sample *NAT*]; Grimes and Al-Ajaj, 1992; Martignago et al., 2003 [sample *H-Cr*]), one high-pressure Brillouin measurement (Speziale et al., 2016) and one high-temperature RPR measurement (Suzuki et al., 2000). The Grüneisen parameter (1.17) was taken from Suzuki et al. (2000) and assumed that it does not vary with temperature. Because the quoted uncertainties of K_{SR} from Suzuki et al. (2000) are substantially smaller than those expected from elasticity measurements (e.g. 1 to 3 GPa), we under-weighted the experimental data (1% esd was assumed for all data). With these constraints, we fitted simultaneously each individual data set with a third-order Birch-Murnaghan compressional EoS in combination with the Holland-Powell thermal-pressure EoS; the final refined EoS parameters (Table 1) fit almost all the data within the experimental uncertainties (Supplementary Material File 1, Figure S3). The final EoS for mantle spinel is provided in Supplementary Material File 4. Considering the bulk modulus systematics for Mg-Fe-Cr-Al spinels, we are confident that our P–V–T–K EoS parameters can be applied to a wide range of Al-rich spinel compositions.

236

237 **2.4 Garnet**

238 Mantle garnets (space group *Ia-3d*, general formula $X_3Y_2Si_3O_{12}$) are multicomponent substitutional
239 solid solutions since different cations can be mutually exchanged at the X (Mg, Fe, Ca, Mn divalent
240 cations) and Y (Al, Fe, Cr trivalent cations) sites. Compositionally, the most significant components
241 of peridotitic garnets are $Mg_3Al_2Si_3O_{12}$ pyrope (ca 75%), $Ca_3Al_2Si_3O_{12}$ grossular (ca 10%) and
242 $Fe_3Al_2Si_3O_{12}$ almandine (ca 15%) (e.g., Wood et al., 2013).

243 The effect of Mg-Fe substitution for the pyrope-almandine solid solution was recently analysed by
244 Lu et al. (2013) and Milani et al. (2015). Milani et al. (2015) determined $K_{TR,0}$ = 163.7(1.7) GPa for
245 pyrope, $K_{TR,0}$ = 167.2(1.7) GPa for an intermediate $Py_{60}Alm_{40}$ and $K_{TR,0}$ = 172.6(1.5) GPa for
246 almandine, with similar $K'_{TR,0}$ for all three garnets, claiming that Fe substituting for Mg linearly
247 increases $K_{TR,0}$ but does not affect $K'_{TR,0}$. However, compared to the sources reviewed by Milani et
248 al. (2015), the determined $K_{TR,0}$ values are notably lower than expected whereas $K'_{TR,0}$ are slightly
249 higher and this can be ascribed to the well-known trade-off between fit values for $K_{TR,0}$ and $K'_{TR,0}$. Lu
250 et al. (2013) measured the elasticity of a Fe-bearing pyrope by high P-T Brillouin spectroscopy,
251 determining $K_{SR,0}$ = 168.2(1.8) and $K'_{SR,0}$ = 4.4(1). Comparative analysis of these results led the
252 authors to conclude that addition of Fe does significantly affect $K_{SR,0}$ but rather has a weak positive
253 effect on $K'_{SR,0}$. A similar conclusion was reached by Jiang et al. (2004), who showed that Fe
254 substituting for Mg in the pyrope-almandine series has a little effect on the bulk modulus (almandine
255 $K_{SR,0}$ being 2% higher than that of pyrope) while it increases its pressure derivative. The effect of Ca-
256 Mg substitution for the pyrope-grossular solid solution has been analysed again by Jiang et al. (2004),
257 who showed that the $K_{SR,0}$ varies by ca 2% across the pyrope-grossular system and that there are no
258 evident trends in the $K'_{SR,0}$. In view of these considerations, we selected data from four different
259 experiments: one compression (Milani et al., 2015 [sample $Py_{60}Alm_{40}$]), two expansions (Bosenick
260 and Geiger, 1997 [excluding the scattered data at 220 K], Milani et al., 2015 [sample Py_{100}]) and one
261 high-temperature RUS measurement (Suzuki and Anderson, 1983). The Grüneisen parameter (1.19)

was taken from Gillet et al. (1992) and assumed that it does not vary with temperature. With these constraints, we fitted simultaneously each individual data set with a third-order Birch-Murnaghan compressional EoS in combination with the Holland-Powell thermal-pressure EoS; the final refined EoS parameters (Table 1) fit all the data within the experimental uncertainties (Supplementary Material File 1, Figure S4). The final EoS for mantle garnet is provided in Supplementary Material File 5. Considering the bulk modulus systematics for Mg-Fe-Ca aluminous garnets, we are confident that our P–V–T–K EoS parameters can be applied to a wide range of mantle garnet compositions.

3. Density variations in the lithospheric mantle

3.1 Density calculations

The density of mantle peridotites is function of the chemical composition, modal abundance and elastic properties of their constituent minerals, which in turn are controlled by pressure, temperature and bulk composition of the system. Here, the density structure of the lithospheric mantle was calculated following a two-step approach.

The first step involved the calculation of density profiles for each phase along the geothermal gradients of interest. To our purposes, three geothermal gradients of 35, 45 and 60 mWm^{-2} were chosen as considered representative of extremely cold, intermediate, and relatively hot lithospheric sections. The density of each phase was calculated in the form of 'crystallographic density' according to the relation:

$$\rho_{(phase\ at\ PT)} = \frac{Z_{(phase)} \times Mw_{(phase)}}{\left(\frac{V}{V0}\right)_{(EoS\ at\ PT)} \times V0_{(phase)} \times Na} \qquad (1)$$

where $\left(\frac{V}{V0}\right)_{(EoS\ at\ PT)}$ represents the volume [here the normalized volume $\left(\frac{V}{V0}\right)$] calculated from the EoS at specific P – T conditions (e.g., for a characteristic geotherm or at any P – T), $V0_{(phase)}$ is the reference unit cell volume of the phase measured at ambient conditions, $Mw_{(phase)}$ its molecular weight, $Z_{(phase)}$ is the number of formula units in the unit cell and Na the Avogadro number.

285 The second step involved the calculation of density profiles for bulk rocks, which were here
286 calculated from the densities ρ_i of n constituent minerals as:

287 $$\rho_{(bulk\ rock)} = \left(\sum_{i=1}^{n} \rho_i \times v_i\right)/n \qquad (2)$$

288 where v_i is the volume proportion of each mineral.

289 We computed density profiles for all constituent mineral phases and for two potential lithospheric
290 mantle sections, a fertile and a depleted peridotitic systems, along the 35, 45 and 60 mWm^{-2}
291 geothermal gradients. Calculations for the two lithospheric sections were restricted to a P – T range
292 of 1 – 8 GPa and 350 – 1375 °C. These gradients were selected from the preferred geotherm family
293 of Hasterok and Chapman (2011), which are based on radiogenic heat production measurements
294 together with xenolith thermobarometry and tectonothermal constraints. Following Hasterok and
295 Chapman (2011), we assumed that the transition from a conductive to an adiabatic geotherm
296 corresponds to the lithosphere-asthenosphere boundary (LAB), which is here used only to discuss the
297 effect of temperature on density profiles.

298 Our calculations at subsolidus conditions do not include the effects of porosity, mineral texture and
299 rock microstructure as well as no volatile-bearing phases, thus excluding OH groups in NAMs and/or
300 intergranular fluids and/or melts.

301 Calculations were based on previously studied natural peridotite xenoliths: a spinel lherzolite from
302 the Veneto Volcanic Province (sample SG34 from Beccaluva et al., 2001) was adopted as
303 representative of a fertile mantle, while a spinel harzburgite from Grande Comore island (sample
304 NDR13, unpublished data from Coltorti et al., 1999), now under investigation for other petrological
305 studies, was chosen to represent a depleted mantle. Modal compositions of the selected samples were
306 calculated by least-squares mass balance using bulk-rock and mineral major element analyses (Tables
307 2, 3).

308 Bearing in mind that calculating the density of each phase requires a reference unit cell volume
309 measured at ambient conditions ($V0_{(phase)}$, equation 1), olivine, pyroxenes, spinel and garnet unit

cell parameters (and related crystal chemical compositions, which slightly differ compared to those expected from our models of fertile and depleted mantle) were selected from literature (Tables 2, 3). Modal compositions were kept from the two selected mantle xenoliths (SG34 spinel lherzolite and NDR13 spinel harzburgite), however density calculations were carried out by using the mineral compositions and unit cell volumes of the reference minerals from the literature. All selected mineral compositions were kept fixed for all density calculations.

The spinel-garnet transition was modelled according to the approximate reaction spinel + pyroxenes = garnet + olivine (e.g., Klemme and O'Neill, 2000); mineral modes in the garnet stability field were calculated from stoichiometric balance upon completion of the reaction (Tables 2, 3). Recent thermodynamic modelling in natural peridotitic systems (Ziberna et al., 2013) indicates that garnet and spinel always coexist and the width and depth of the coexistence interval strongly, but not only, depends on the thermal state of the lithosphere (restricted depth interval - about 15 km - in regions with hot geotherms, and much broader interval - over 100 km - for cold geotherms). We simplified this model by assuming garnet + spinel coexistence intervals of 1.5 – 4 GPa, 1.5 – 3 GPa and 1.8 – 2.4 GPa along the 35, 45 and 60 mWm^{-2} geothermal gradients, respectively, for both fertile and depleted mantle sections. For density calculations, mineral modes were kept fixed in spinel and garnet stability fields, and were imposed to vary linearly in the spinel-garnet stability field.

3.2 Results

Density profiles for both mineral phases and the fertile and depleted peridotitic systems were calculated along three different geothermal gradients: 35 mWm^{-2} (Figures 1, 2), representative of the coldest cratonic mantle sections, 45 mWm^{-2} (Figures 1, 3), typical of average cratonic sections, and 60 mWm^{-2} (Figures 1, 4), for relatively hot, off-craton, lithospheric sections (Hasterok and Chapman, 2011).

Figure 1 shows that, despite mineral phases having different elastic parameters (Table 1), their density variation with depth is largely controlled by the geothermal gradients. Under cold conditions (35

336 mWm^{-2}), density curves for all phases shows a subtle but significant decrease down to ca 1 GPa,
337 which is followed by a marked increase for olivine and pyroxenes and a moderate increase for spinel,
338 magnesiochromite and garnet. Under relatively hot conditions (60 mWm^{-2}), density curves for all
339 phases exhibit a marked decrease down to ca 3 GPa, followed by an increase with depth. It is under
340 intermediate conditions (45 mWm^{-2}) and at P > 1 GPa that density curves exhibit most of the
341 differences. Indeed, density curves for all mineral phases show a gentle decrease down to ca 1 GPa,
342 where the density of olivine and pyroxenes starts to increase, whereas it continues to decrease down
343 to ca 4.5 GPa for spinel, magnesiochromite and garnet. Such distinct behaviour is clearly due to
344 different elastic parameters (Table 1), but it is also due to the interplay between increasing
345 temperature and pressure, whose effects are of the same order (see also considerations below).
346 Noteworthy errors associated with density calculations through the newly developed and two selected
347 EoS are minimum (Figure 1), and this in turn affects the accuracy of density profiles for bulk rocks.
348 Such errors, esd($\rho/\rho 0$) ~ 10^{-3}, translate to uncertainties of density calculations which are ~ 0.05 %
349 (e.g., 3.416(2) g/cm^3 or conversely 3416(2) kg/m^3 at ~ 6 GPa and ~1050 °C for the fertile peridotitic
350 system), which are considerably much less than average uncertainties associated to density
351 calculations.
352 If we consider a geotherm of 35 mWm^{-2} and both fertile and depleted compositions (Figure 2), the
353 density in the mantle shows a similar behaviour, progressively increasing with increasing depth. This
354 indicates that the effect of pressure prevails over that of the slowly rising temperature. By comparing
355 the trends of the fertile and depleted mantle sections (Figure 5), it is evident that the former is typified
356 by a more pronounced density increase with respect to the depleted one. This is attributable to the
357 higher modes of garnet (due to higher bulk Al_2O_3 in fertile compositions), which is among the densest
358 mineral phases in peridotite assemblages (e.g., Lee, 2003).
359 If we consider a geotherm of 45 mWm^{-2}, results are somehow different in the 1-4 GPa interval. Here,
360 the density of the depleted peridotitic system remains nearly constant while it moderately increases
361 for the fertile system; then the density of both systems increases from 4 down to 8 GPa (Figures 3,

362 5). These results suggest that (i) the effect of temperature on the evolution of the bulk density with
363 depth is comparable to that of pressure and that (ii) the behaviour of the two systems is decoupled
364 down to ca 4 GPa.
365 If we consider a relatively hot geotherm of 60 mWm^{-2}, the temperature increase with depth is so
366 strong that leads to an overall decrease of the bulk density of both depleted and fertile systems in the
367 lithosphere from 1 to about 3 GPa, followed by an increase from 3 down to 8 GPa (Figure 4). By
368 comparing the trends of the two sections (Figure 5), the fertile system shows a more gentle decrease
369 in its density compared to the depleted system. This is again attributable to the higher modes of garnet,
370 which, combined with the P – T gradient effects, result in a slightly smoother density profile.
371 Irrespective of the specific depth and width of their coexistence intervals, spinel and garnet have a
372 stronger control on the density variations in case of fertile compositions, due to their higher modes.
373
374 **3.3 Discussion**
375 **3.3.1 Density models and the effect of the thermal state**
376 Most of the recently published upper mantle density models derive from phase equilibria calculations
377 based on thermodynamic data, where stable mineral assemblages are computed using Gibbs free-
378 energy minimization techniques. Previous works (Fullea et al., 2014; Ziberna and Klemme, 2016)
379 showed some contrasting results as to whether the lithospheric density is predominantly controlled
380 by the thermal state, bulk composition, or their interplay. Fullea et al. (2014) unravelled the present-
381 day Irish lithospheric structure through LitMod3D code (Fullea et al., 2009) that combines
382 petrological and geophysical observations with thermodynamic data (in the CFMAS system) within
383 a self-consistent framework. This modelling revealed similar vertical density profiles - sharp spinel
384 – garnet phase transition with an abrupt increase of density, a general trend of decreasing density
385 down to ~ 100 km, followed by an increase (Figure 5) - associated with all the mantle compositions
386 discussed in the work (i.e., from fertile to moderately depleted peridotites). Overall, these density
387 trends suggest a greater control of the thermal state on the lithospheric density rather than bulk

388 composition in the Irish lithosphere (60 to 70 mWm^{-2}). Considering the lack of Cr (for which there is
389 evidence that it may considerably change phase relations in the upper mantle) in most previous
390 calculations, Ziberna and Klemme (2016) investigated the density variations for Cr-bearing mantle
391 compositions (Pali-Aike xenoliths, Patagonia) in response to changes in bulk compositions and
392 thermal gradients by means of well-established free energy minimization techniques, with
393 thermodynamic calculations based on the internally consistent dataset of Holland and Powell (1998)
394 complemented for the most relevant Cr-bearing phases in the upper mantle (Ziberna et al., 2013).
395 Contrary to previous results (Fullea et al., 2014), this work showed that the density profiles across
396 the spinel – garnet peridotite transition are not sharp and depend both on bulk composition (especially
397 on Al_2O_3 and Cr_2O_3) and geothermal gradient (Figure 5). Moreover, while under relatively hot
398 thermal conditions (70 mWm^{-2}) density profiles for both fertile and depleted compositions show
399 similar trends (i.e., density decrease down to ca 2.5 GPa), this is not the case for intermediate thermal
400 conditions (50 mWm^{-2}) where density in the mantle for depleted compositions remains virtually
401 constant down to ca 4 GPa and it rapidly increases for more fertile compositions (Figure 5).
402 Accordingly, these authors suggested that it is the interplay between bulk composition and thermal
403 gradient that controls density variations in the lithospheric mantle.
404 Our models predict a much greater thermal control over the density of the lithospheric mantle, with
405 some compositional control mostly arising at cold-intermediate thermal conditions (Figure 5).
406 Considering that we based the spinel – garnet phase transitions on Ziberna et al. (2013)
407 thermodynamic model (cfr. Section 3.1), spinel and garnet coexist over a significant depth interval.
408 Accordingly, our models predict a smooth variation of densities across the spinel – garnet transition
409 and no abrupt changes. As already evidenced by Ziberna and Klemme (2016), the sharp spinel –
410 garnet transitions associated with an abrupt change of density identified by Fullea et al. (2014) can
411 be ascribed to the lack of Cr in their thermodynamic model. If this aspect is ruled out from further
412 discussion, and density curves are analysed overall, there are some similarities with those from Fullea
413 et al. (2014) (Figure 5). Indeed, all modelled compositions exhibit an overall decrease of the bulk

density up to about 100 km, followed by an increase downwards, for relatively hot thermal conditions (60 to 70 mWm^{-2}). Our density curves show even more striking similarities with those from Ziberna and Klemme (2016), for which a similar behaviour is predicted for fertile and depleted compositions under relatively hot thermal conditions (70 mWm^{-2}), and a different one under intermediate conditions (50 mWm^{-2}) (Figure 5). Therefore, our investigation shows that density profiles in natural systems with simplified phase relations display comparable trends to those reported in previous studies. In this framework, perspectives are that the thermal gradient exerts substantial control when it comes to the density structure of the lithosphere and that the compositional control on the density evolution with depth may be less than previously suggested. In the next section, we show how density calculations based on simplified phase relations can be reconciled with Perple_X-based results from previous literature. We also infer the thermal gradient is the main controlling variable of the lithospheric mantle density.

3.3.2 Comparison between Perple_X and simplified calculations

Although a strict evaluation of similarities and differences of our simplified parameterisation for calculating density variations with respect to classic thermodynamic modelling (e.g., Perple_X) goes beyond the scope of this paper (detailed results of the application of both models to a real mantle section will be presented elsewhere), in the following we provide an application of our model compared with previous results from literature (Ziberna and Klemme, 2016). To this aim, we selected two of the four representative mantle xenoliths from Pali-Aike, Patagonia, reported in Ziberna and Klemme (2016), namely PA3 (spinel harzburgite) and BN4 (spinel-garnet lherzolite), for which we computed density profiles along the 50 and 70 mWm^{-2} geothermal gradients (Figure 6). Input data for Ziberna and Klemme (2016) thermodynamic modelling are whole-rock analyses from Stern et al. (1999), with calculations performed in the SiO_2-Al_2O_3-Cr_2O_3-FeO-MgO-CaO-Na_2O system. In order to provide a clear and consistent comparison between the two methods, input data (i.e., mineral

compositions and modes) for our simplified parameterisation were as follows. Olivine, pyroxenes, and spinel mineral compositions and modes were selected from Perple_X calculations of Ziberna and Klemme (2016) at 1 GPa (at the corresponding temperature for the 50 and 70 mWm^{-2} geothermal gradients). Garnet compositions were selected from Perple_X calculations of Ziberna and Klemme (2016) at P – T corresponding to spinel-out reaction (which depends on bulk composition and geothermal gradient); garnet, as well as olivine and pyroxenes modes in the garnet stability field, were calculated from stoichiometric balance upon completion of the reaction spinel + pyroxenes = garnet + olivine, using the selected mineral modes and compositions. Selected mineral compositions were kept fixed along the whole section; mineral modes were kept fixed in spinel and garnet stability fields, and were imposed to vary linearly in the spinel-garnet stability field (cfr. Section 3.1). Depth intervals of coexistence of spinel + garnet were selected again from Perple_X calculations of Ziberna and Klemme (2016). Density variations with depth and thermal regime for PA3 (spinel harzburgite) and BN4 (spinel-garnet lherzolite) mantle xenoliths are reported in Figure 6, along with original curves from Ziberna and Klemme (2016).

Note that Ziberna and Klemme (2016) thermodynamic model considered phase equilibria, with mineral modes and compositions continuously changing according to P – T conditions, which has not been done in this study. Nonetheless, density curves calculated with our simplified parameterisation match well those from Ziberna and Klemme (2016), both in their general trends with depth and absolute values, with a maximum difference between the two models of ca 20 kg/m^3 (Figure 6). From this similarity, we conclude that our approach with simplified phase relations has enough accuracy for investigating the density structure of the lithosphere. We also infer that the density structure of the lithospheric mantle is predominantly controlled by the thermal gradient variations, with most of the compositional control arising at cold-intermediate thermal conditions. No less importantly, we showed that the newly developed P–V–T–K EoS (pyroxenes, spinel and garnet) in combination with the published EoS for mantle olivine and mantle magnesiochromite are applicable for calculating the

density of mantle peridotites and its variation, with minimum uncertainties, under different thermal regimes and bulk compositions, without requiring sets of end-member properties and solution models.

4. Concluding remarks

In this study, we presented an assessment of the thermoelastic parameters of orthopyroxene, clinopyroxene, spinel and garnet based on X-Ray diffraction data and direct elastic measurements available in literature. The newly developed EoS consistently describe the elastic behaviour of these phases under the most relevant P–T conditions and bulk compositions of the Earth's mantle, along with the published EoS for mantle olivine and magnesiochromite.

As a case study, we evaluated the influence of bulk composition and thermal regimes on the density structure of potential lithospheric mantle sections, following a simplified parameterisation that does not incorporate phase relations. Accordingly, density profiles for fertile and depleted peridotitic systems based on the EoS of their constituent mineral phases were calculated for three different geothermal gradients (35, 45 and 60 mWm^{-2}), for a P – T range of 1 – 8 GPa and 350 – 1375 °C. In case of very cold geotherms (35 mWm^{-2}), the density of both depleted and fertile systems progressively increases with increasing depth. In case of intermediate geotherms (45 mWm^{-2}), the density of a depleted peridotitic system remains nearly constant up to about 4 GPa, while it moderately increases in a fertile system, due to higher modes of garnet. In case of relatively hot geotherms (60 mWm^{-2}), the density of both depleted and fertile systems progressively decreases with increasing depth, up to about 3 GPa, and then increases downwards. Moreover, we also provided an example of application of our model in comparison with classic thermodynamic modelling results from literature. From such comparison, we concluded that (i) density profiles for mantle sections can be computed with enough accuracy following our simplified parameterisation, (ii) the thermal gradient exerts substantial control when it comes to the density structure of the lithosphere and (iii) the compositional control on the density evolution with depth may be less than previously suggested.

Funding

L.F. acknowledges Istituto Nazionale di Geofisica e Vulcanologia (INGV) for funding his Ph.D. project (XXXV cycle) with thematic ‘Links between rheology, mineralogy and composition of the Earth's mantle’ and the Italian National Research Program (PRIN Grant 20178LPCPW ’Micro to Macro - How to unravel the nature of the Large Magmatic Events' to [M.C.])

Acknowledgements

Dr. Luca Ziberna is thanked for providing work files that allowed a validation of our simplified parameterisation for calculating density variations with respect to Perple_X models. The authors are grateful to Michel Grégoire and an anonymous reviewer for their constructive comments, which improved an earlier version of the manuscript. Michael Roden is acknowledged for his careful editorial handling and guidance.

References

Abers, G.A., Hacker, B.R., 2016. A MATLAB toolbox and Excel workbook for calculating the densities, seismic wave speeds, and major element composition of minerals and rocks at pressure and temperature. Geochemistry, Geophys. Geosystems 17, 616–624. https://doi.org/10.1002/2015GC006171

Afonso, J.C., Fernàndez, M., Ranalli, G., Griffin, W.L., Connolly, J.A.D., 2008. Integrated geophysical-petrological modeling of the lithosphere and sublithospheric upper mantle: Methodology and applications. Geochemistry, Geophys. Geosystems 9, Q05008. https://doi.org/10.1029/2007GC001834

Afonso, J.C., Fullea, J., Yang, Y., Connolly, J.A.D., Jones, A.G., 2013. 3-D multi-observable probabilistic inversion for the compositional and thermal structure of the lithosphere and upper mantle. II: General methodology and resolution analysis. J. Geophys. Res. Solid Earth 118,

513 1650–1676. https://doi.org/10.1002/jgrb.50123

514 Afonso, J.C., Ranalli, G., Fernàndez, M., 2007. Density structure and buoyancy of the oceanic
515 lithosphere revisited. Geophys. Res. Lett. 34, 2–6. https://doi.org/10.1029/2007GL029515

516 Anderson, O.L., 1995. Equations of state of solids for geophysics and ceramic science, Oxford
517 Monographs on Geology and Geophysics. https://doi.org/10.1016/0016-7037(95)90195-7

518 Angel, R.J., 2000. Equations of State. Rev. Mineral. Geochemistry 41, 35–59.
519 https://doi.org/10.2138/rmg.2000.41.2

520 Angel, R.J., Alvaro, M., Gonzalez-Platas, J., 2014. EosFit7c and a Fortran module (library) for
521 equation of state calculations. Zeitschrift für Krist. - Cryst. Mater. 229, 405–419.
522 https://doi.org/10.1515/zkri-2013-1711

523 Angel, R.J., Alvaro, M., Nestola, F., 2018. 40 years of mineral elasticity: a critical review and a new
524 parameterisation of equations of state for mantle olivines and diamond inclusions. Phys. Chem.
525 Miner. 45, 95–113. https://doi.org/10.1007/s00269-017-0900-7

526 Angel, R.J., Jackson, J.M., 2002. Elasticity and equation of state of orthoenstatite, MgSiO 3. Am.
527 Mineral. 87, 558–561. https://doi.org/10.2138/am-2002-0419

528 Bass, J.D., Anderson, D.L., 1984. Composition of the upper mantle: Geophysical tests of two
529 petrological models. Geophys. Res. Lett. 11, 229–232.
530 https://doi.org/10.1029/GL011i003p00229

531 Beccaluva, L., Bonadiman, C., Coltorti, M., Salvini, L., Siena, F., 2001. Depletion Events, Nature
532 of Metasomatizing Agent and Timing of Enrichment Processes in Lithospheric Mantle
533 Xenoliths from the Veneto Volcanic Province. J. Petrol. 42, 173–188.
534 https://doi.org/10.1093/petrology/42.1.173

535 Bosenick, A., Geiger, C.A., 1997. Powder X ray diffraction study of synthetic pyrope-grossular

garnets between 20 and 295 K. J. Geophys. Res. Solid Earth 102, 22649–22657. https://doi.org/10.1029/97JB01612

Braun, J., 2010. The many surface expressions of mantle dynamics. Nat. Geosci. 3, 825–833. https://doi.org/10.1038/ngeo1020

Cameron, M., Sueno, S., Prewitt, C.T., Papike, J.J., 1973. High-Temperature crystal chemistry of acmite, diopside, hedenbergite, jadeite, spodumene, and Ureyite. Am. Mineral. 58, 594–618.

Capitanio, F., Morra, G., Goes, S., 2007. Dynamic models of downgoing plate-buoyancy driven subduction: Subduction motions and energy dissipation. Earth Planet. Sci. Lett. 262, 284–297. https://doi.org/10.1016/j.epsl.2007.07.039

Carbonin, S., Martignago, F., Menegazzo, G., Dal Negro, A., 2002. X-ray single-crystal study of spinels: in situ heating. Phys. Chem. Miner. 29, 503–514. https://doi.org/10.1007/s00269-002-0262-6

Chai, M., Brown, J.M., Slutsky, L.J., 1997. The elastic constants of an aluminous orthopyroxene to 12.5 GPa. J. Geophys. Res. Solid Earth 102, 14779–14785. https://doi.org/10.1029/97JB00893

Coltorti, M., Bonadiman, C., Casetta, F., Faccini, B., Giacomoni, P.P., Pelorosso, B., Perinelli, C., 2021. Nature and evolution of the northern Victoria Land lithospheric mantle (Antarctica) as revealed by ultramafic xenoliths. Geol. Soc. London, Mem. 56, M56-2020–11. https://doi.org/10.1144/M56-2020-11

Coltorti, M., Bonadiman, C., Hinton, R.W., Siena, F., Upton, B.G.J., 1999. Carbonatite Metasomatism of the Oceanic Upper Mantle: Evidence from Clinopyroxenes and Glasses in Ultramafic Xenoliths of Grande Comore, Indian Ocean. J. Petrol. 40, 133–165. https://doi.org/10.1093/petroj/40.1.133

Connolly, J.A.D., 2009. The geodynamic equation of state: What and how. Geochemistry, Geophys.

559 Geosystems 10, Q10014. https://doi.org/10.1029/2009GC002540

560 Connolly, J.A.D., Petrini, K., 2002. An automated strategy for calculation of phase diagram sections
561 and retrieval of rock properties as a function of physical conditions. J. Metamorph. Geol. 20,
562 697–708. https://doi.org/10.1046/j.1525-1314.2002.00398.x

563 Fullea, J., Afonso, J.C., Connolly, J.A.D., Fernàndez, M., García-Castellanos, D., Zeyen, H., 2009.
564 LitMod3D: An interactive 3-D software to model the thermal, compositional, density,
565 seismological, and rheological structure of the lithosphere and sublithospheric upper mantle.
566 Geochemistry, Geophys. Geosystems 10. https://doi.org/10.1029/2009GC002391

567 Fullea, J., Muller, M.R., Jones, A.G., Afonso, J.C., 2014. The lithosphere–asthenosphere system
568 beneath Ireland from integrated geophysical–petrological modeling II: 3D thermal and
569 compositional structure. Lithos 189, 49–64. https://doi.org/10.1016/j.lithos.2013.09.014

570 Gillet, P., Fiquetw, G., Malézieux, J.M., Geiger, C.A., 1992. High-pressure and high-temperature
571 Raman spectroscopy of end-member garnets: pyrope, grossular and andradite. Eur. J. Mineral.
572 4, 651–664. https://doi.org/10.1127/ejm/4/4/0651

573 Grimes, N.W., Al-Ajaj, E.A., 1992. Low-temperature thermal expansion of spinel. J. Phys.
574 Condens. Matter 4, 6375–6380. https://doi.org/10.1088/0953-8984/4/30/004

575 Hacker, B.R., Abers, G.A., 2004. Subduction Factory 3: An Excel worksheet and macro for
576 calculating the densities, seismic wave speeds, and H 2 O contents of minerals and rocks at
577 pressure and temperature. Geochemistry, Geophys. Geosystems 5, n/a-n/a.
578 https://doi.org/10.1029/2003GC000614

579 Hasterok, D., Chapman, D.S., 2011. Heat production and geotherms for the continental lithosphere.
580 Earth Planet. Sci. Lett. 307, 59–70. https://doi.org/10.1016/j.epsl.2011.04.034

581 Holland, T.J.B., Powell, R., 2011. An improved and extended internally consistent thermodynamic

582 dataset for phases of petrological interest, involving a new equation of state for solids. J.
583 Metamorph. Geol. 29, 333–383. https://doi.org/10.1111/j.1525-1314.2010.00923.x

584 Holland, T.J.B., Powell, R., 1998. An internally consistent thermodynamic data set for phases of
585 petrological interest. J. Metamorph. Geol. 16, 309–343. https://doi.org/10.1111/j.1525-
586 1314.1998.00140.x

587 Hugh-Jones, D., Chopelas, A., Augel, R., 1997. Tetrahedral compression in (Mg,Fe)SiO 3
588 orthopyroxenes. Phys. Chem. Miner. 24, 301–310. https://doi.org/10.1007/s002690050042

589 Hugh-Jones, D.A., Angel, R.J., 1997. Effect of Ca 2+ and Fe 2+ on the equation of state of MgSiO
590 3 orthopyroxene. J. Geophys. Res. Solid Earth 102, 12333–12340.
591 https://doi.org/10.1029/96JB03485

592 Isaak, D.G., Ohno, I., Lee, P.C., 2006. The elastic constants of monoclinic single-crystal chrome-
593 diopside to 1,300 K. Phys. Chem. Miner. 32, 691–699. https://doi.org/10.1007/s00269-005-
594 0047-9

595 Jiang, F., Speziale, S., Duffy, T.S., 2004. Single-crystal elasticity of grossular- and almandine-rich
596 garnets to 11 GPa by Brillouin scattering. J. Geophys. Res. Solid Earth 109, 1–10.
597 https://doi.org/10.1029/2004JB003081

598 Klemme, S., O'Neill, H.S., 2000. The near-solidus transition from garnet lherzolite to spinel
599 lherzolite. Contrib. to Mineral. Petrol. 138, 237–248. https://doi.org/10.1007/s004100050560

600 Lee, C.-T.A., 2003. Compositional variation of density and seismic velocities in natural peridotites
601 at STP conditions: Implications for seismic imaging of compositional heterogeneities in the
602 upper mantle. J. Geophys. Res. Solid Earth 108, 2441. https://doi.org/10.1029/2003JB002413

603 Li, B., Neuville, D.R., 2010. Elasticity of diopside to 8GPa and 1073K and implications for the
604 upper mantle. Phys. Earth Planet. Inter. 183, 398–403.

https://doi.org/10.1016/j.pepi.2010.08.009

Lu, C., Mao, Z., Lin, J.-F., Zhuravlev, K.K., Tkachev, S.N., Prakapenka, V.B., 2013. Elasticity of single-crystal iron-bearing pyrope up to 20GPa and 750K. Earth Planet. Sci. Lett. 361, 134–142. https://doi.org/10.1016/j.epsl.2012.11.041

Martignago, F., Negro, A.D., Carbonin, S., 2003. How Cr3+ and Fe3+ affect Mg?Al order?disorder transformation at high temperature in natural spinels. Phys. Chem. Miner. 30, 401–408. https://doi.org/10.1007/s00269-003-0336-0

Mazzucchelli, M., Rivalenti, G., Brunelli, D., Zanetti, A., Boari, E., 2009. Formation of Highly Refractory Dunite by Focused Percolation of Pyroxenite-Derived Melt in the Balmuccia Peridotite Massif (Italy). J. Petrol. 50, 1205–1233. https://doi.org/10.1093/petrology/egn053

McDonough, W.F., Rudnick, R.L., 1998. Mineralogy and composition of the upper mantle, in: Reviews in Mineralogy, Vol. 37. pp. 139–164.

Melchiorre, M., Faccini, B., Grégoire, M., Benoit, M., Casetta, F., Coltorti, M., 2020. Melting and metasomatism/refertilisation processes in the Patagonian sub-continental lithospheric mantle: A review. Lithos 354–355, 105324. https://doi.org/10.1016/j.lithos.2019.105324

Milani, S., Angel, R.J., Scandolo, L., Mazzucchelli, M.L., Ballaran, T.B., Klemme, S., Domeneghetti, M.C., Miletich, R., Scheidl, K.S., Derzsi, M., Tokár, K., Prencipe, M., Alvaro, M., Nestola, F., 2017. Thermo-elastic behavior of grossular garnet at high pressures and temperatures. Am. Mineral. 102, 851–859. https://doi.org/10.2138/am-2017-5855

Milani, S., Nestola, F., Alvaro, M., Pasqual, D., Mazzucchelli, M.L., Domeneghetti, M.C., Geiger, C.A., 2015. Diamond–garnet geobarometry: The role of garnet compressibility and expansivity. Lithos 227, 140–147. https://doi.org/10.1016/j.lithos.2015.03.017

Nestola, F., Ballaran, T.B., Balic-Zunic, T., Princivalle, F., Secco, L., Dal Negro, A., 2007.

628 Comparative compressibility and structural behavior of spinel MgAl2O4 at high pressures:
629 The independency on the degree of cation order. Am. Mineral. 92, 1838–1843.
630 https://doi.org/10.2138/am.2007.2573

631 Nestola, F., Periotto, B., Anzolini, C., Andreozzi, G.B., Woodland, A.B., Lenaz, D., Alvaro, M.,
632 Princivalle, F., 2015. Equation of state of hercynite, FeAl2O4, and high-pressure systematics
633 of Mg-Fe-Cr-Al spinels. Mineral. Mag. 79, 285–294.
634 https://doi.org/10.1180/minmag.2015.079.2.07

635 Nestola, F., Zaffiro, G., Mazzucchelli, M.L., Nimis, P., Andreozzi, G.B., Periotto, B., Princivalle,
636 F., Lenaz, D., Secco, L., Pasqualetto, L., Logvinova, A.M., Sobolev, N. V, Lorenzetti, A.,
637 Harris, J.W., 2019. Diamond-inclusion system recording old deep lithosphere conditions at
638 Udachnaya (Siberia). Sci. Rep. 9, 12586. https://doi.org/10.1038/s41598-019-48778-x

639 Pandolfo, F., Cámara, F., Domeneghetti, M.C., Alvaro, M., Nestola, F., Karato, S.-I., Amulele, G.,
640 2015. Volume thermal expansion along the jadeite–diopside join. Phys. Chem. Miner. 42, 1–
641 14. https://doi.org/10.1007/s00269-014-0694-9

642 Pearson, D.G., Canil, D., Shirey, S.B., 2003. Mantle Samples Included in Volcanic Rocks:
643 Xenoliths and Diamonds, in: Treatise on Geochemistry. Elsevier, pp. 171–275.
644 https://doi.org/10.1016/B0-08-043751-6/02005-3

645 Prencipe, M., Tribaudino, M., Pavese, A., Hoser, A., Reehuis, M., 2000. A SINGLE-CRYSTAL
646 NEUTRON-DIFFRACTION INVESTIGATION OF DIOPSIDE AT 10 K. Can. Mineral. 38,
647 183–189. https://doi.org/10.2113/gscanmin.38.1.183

648 Sang, L., Bass, J.D., 2014. Single-crystal elasticity of diopside to 14GPa by Brillouin scattering.
649 Phys. Earth Planet. Inter. 228, 75–79. https://doi.org/10.1016/j.pepi.2013.12.011

650 Scandolo, L., Mazzucchelli, M.L., Alvaro, M., Nestola, F., Pandolfo, F., Domeneghetti, M.C., 2015.
651 Thermal expansion behaviour of orthopyroxenes: the role of the Fe-Mn substitution. Mineral.

652 Mag. 79, 71–87. https://doi.org/10.1180/minmag.2015.079.1.07

653 Schutt, D.L., Lesher, C.E., 2006. Effects of melt depletion on the density and seismic velocity of
654 garnet and spinel lherzolite. J. Geophys. Res. Solid Earth 111.
655 https://doi.org/10.1029/2003JB002950

656 Simon, N.S.C., Podladchikov, Y.Y., 2008. The effect of mantle composition on density in the
657 extending lithosphere. Earth Planet. Sci. Lett. 272, 148–157.
658 https://doi.org/10.1016/j.epsl.2008.04.027

659 Speziale, S., Nestola, F., Jiang, F., Duffy, T.S., 2016. Single-crystal elastic constants of spinel
660 (MgAl2O4) to 11.1 GPa by Brillouin scattering, in: AGU Fall Meeting Abstracts. pp. MR23A-
661 2658.

662 Stern, C.R., Kilian, R., Olker, B., Hauri, E.H., Kurtis Kyser, T., 1999. Evidence from mantle
663 xenoliths for relatively thin (<100 km) continental lithosphere below the Phanerozoic crust of
664 southernmost South America. Lithos 48, 217–235. https://doi.org/10.1016/S0419-
665 0254(99)80013-5

666 Stixrude, L., Lithgow-Bertelloni, C., 2011. Thermodynamics of mantle minerals - II. Phase
667 equilibria. Geophys. J. Int. 184, 1180–1213. https://doi.org/10.1111/j.1365-
668 246X.2010.04890.x

669 Stixrude, L., Lithgow-Bertelloni, C., 2005a. Mineralogy and elasticity of the oceanic upper mantle:
670 Origin of the low-velocity zone. J. Geophys. Res. 110, B03204.
671 https://doi.org/10.1029/2004JB002965

672 Stixrude, L., Lithgow-Bertelloni, C., 2005b. Thermodynamics of mantle minerals - I. Physical
673 properties. Geophys. J. Int. 162, 610–632. https://doi.org/10.1111/j.1365-246X.2005.02642.x

674 Suzuki, I., Anderson, O.L., 1983. Elasticity and thermal expansion of a natural garnet up to 1,000K.

675 J. Phys. Earth 31, 125–138. https://doi.org/10.4294/jpe1952.31.125

676 Suzuki, I., Ohno, I., Anderson, O.L., 2000. Harmonic and anharmonic properties of spinel MgAl 2
677 O 4. Am. Mineral. 85, 304–311. https://doi.org/10.2138/am-2000-2-307

678 Thybo, H., Artemieva, I.M., 2013. Moho and magmatic underplating in continental lithosphere.
679 Tectonophysics 609, 605–619. https://doi.org/10.1016/j.tecto.2013.05.032

680 Wood, B.J., Kiseeva, E.S., Matzen, A.K., 2013. Garnet in the Earth's Mantle. Elements 9, 421–426.
681 https://doi.org/10.2113/gselements.9.6.421

682 Xu, J., Zhang, D., Dera, P., Zhang, B., Fan, D., 2017. Experimental evidence for the survival of
683 augite to transition zone depths, and implications for subduction zone dynamics. Am. Mineral.
684 102, 1516–1524. https://doi.org/10.2138/am-2017-5959

685 Xu, Z., Ma, M., Li, B., Hong, X., 2019. Compressibility and thermal expansion of natural
686 clinopyroxene Di0.66Hd0.13Jd0.12Ts0.05. Results Phys. 12, 447–453.
687 https://doi.org/10.1016/j.rinp.2018.11.077

688 Yang, H., Ghose, S., 1994. Thermal expansion, Debye temperature and Gruneisen parameter of
689 synthetic (Fe, Mg)SiO3 orthopyroxenes. Phys. Chem. Miner. 20, 575–586.
690 https://doi.org/10.1007/BF00211853

691 Zhang, J.S., Bass, J.D., 2016. Single-crystal elasticity of natural Fe-bearing orthoenstatite across a
692 high-pressure phase transition. Geophys. Res. Lett. 43, 8473–8481.
693 https://doi.org/10.1002/2016GL069963

694 Ziberna, L., Klemme, S., 2016. Application of thermodynamic modelling to natural mantle
695 xenoliths: examples of density variations and pressure–temperature evolution of the
696 lithospheric mantle. Contrib. to Mineral. Petrol. 171, 16. https://doi.org/10.1007/s00410-016-
697 1229-9

Ziberna, L., Klemme, S., Nimis, P., 2013. Garnet and spinel in fertile and depleted mantle: insights from thermodynamic modelling. Contrib. to Mineral. Petrol. 166, 411–421. https://doi.org/10.1007/s00410-013-0882-5

Figure captions

Figure 1. Density profiles (ρ/ρ0) for mineral phases in the studied peridotitic systems (olivine, orthopyroxene, clinopyroxene, spinel, magnesiochromite and garnet) calculated along a 35 mWm^{-2} geotherm (blue curves), 45 mWm^{-2} geotherm (yellow curves) and 60 mWm^{-2} geotherm (red curves). The 35, 45 and 60 mWm^{-2} conductive geotherms for density calculations are from Hasterok and Chapman (2011). Esd(ρ/ρ0) (estimated standard deviation) refers to the uncertainties associated with EoS fitting (as calculated by the least-squares method) and density calculations. Note that these uncertainties are minimum.

Figure 2. Density profiles for fertile (left panel) and depleted (right panel) peridotitic systems calculated along a 35 mWm^{-2} geotherm. Brown to yellow colour bar represents the density variations along the profiles. Grey lines subdivide the ideal mantle sections into the spinel, spinel + garnet and garnet stability fields, following a simplification of Ziberna et al. (2013) thermodynamic model. The iso-density line for $\rho = 3.40$ g/cm^3 is shown for reference.

Figure 3. Density profiles for fertile (left panel) and depleted (right panel) peridotitic systems calculated along a 45 mWm^{-2} geotherm. Brown to yellow colour bar represents the density variations along the profiles. Grey lines subdivide the ideal mantle sections into the spinel, spinel + garnet and garnet stability fields, following a simplification of Ziberna et al. (2013) thermodynamic model. The iso-density line for $\rho = 3.40$ g/cm^3 is shown for reference.

Figure 4. Density profiles for fertile (left panel) and depleted (right panel) peridotitic systems calculated along a 60 mWm^{-2} geotherm. Brown to yellow colour bar represents the density variations along the profiles. Grey lines subdivide the ideal mantle sections into the spinel, spinel + garnet and garnet stability fields, following a simplification of Ziberna et al. (2013) thermodynamic model. The iso-density line for $\rho = 3.40$ g/cm^3 is shown for reference.

Figure 5. Comparison of density profiles for fertile (left panel) and depleted (right panel) peridotitic systems calculated along a 35 mWm^{-2} geotherm (blue curves), 45 mWm^{-2} geotherm (yellow curves) and 60 mWm^{-2} geotherm (red curves). Density curves from previous literature are also shown: av. Lh (70 mWm^{-2}), av. Lh (50 mWm^{-2}), av. Hz (70 mWm^{-2}) and av. Hz (50 mWm^{-2}) are respectively the average density curves for fertile (TM16, BN4) and depleted (LS1, PA3) mantle xenoliths from Ziberna and Klemme (2016) calculated along the 70 mWm^{-2} and 50 mWm^{-2} geothermal gradients, whereas Inv. Lh (60-70 mWm^{-2}) and Inv. Hz (60-70 mWm^{-2}) are respectively the density curves of Inver lherzolite and harzburgite mantle xenoliths from Fullea et al. (2014) calculated under the Irish thermal state (60 to 70 mWm^{-2}).

Figure 6. Density profiles for PA3 (spinel harzburgite) and BN4 (spinel-garnet lherzolite) mantle xenoliths calculated along the 50 and 70 mWm^{-2} geothermal gradients following our simplified parameterisation in comparison with Perple_X-based original curves from Ziberna and Klemme (2016). Note the similarities between the two distinct sets of curves, both in their general trends and absolute values, as the density difference is always < 20 kg/m^3.

EoS of mantle minerals coupled with composition and thermal state of the lithosphere: inferring the density structure of peridotitic systems

Luca Faccincani[1,*], Barbara Faccini[1], Federico Casetta[1,2], Maurizio Mazzucchelli[3], Fabrizio Nestola[4] and Massimo Coltorti[1,5]

[1] *Department of Physics and Earth Sciences, University of Ferrara, Via Saragat 1, 44121 Ferrara, Italy*

[2] *Department of Lithospheric Research, University of Vienna, Althanstraße 14, 1090 Vienna, Austria*

[3] *Department of Chemical and Geological Sciences, University of Modena and Reggio Emilia, Via Campi 103, 41125 Modena, Italy*

[4] *Department of Geosciences, University of Padua, Via Gradenigo 6, 35131 Padua, Italy*

[5] *Istituto Nazionale di Geofisica e Vulcanologia (INGV) Sezione di Palermo, Via Ugo la Malfa 153, 90146 Palermo, Italy*

*** Corresponding author:** Luca Faccincani; email: luca.faccincani@unife.it

Abstract

Unravelling the physical state and properties of mantle rocks is crucial for understanding both plate tectonics, seismic activity, and volcanism. In this context, the knowledge of accurate elastic parameters of constituent mineral phases, and their variations with pressure (P) and temperature (T), is an essential requirement, that coupled with the thermal state of the lithosphere can provide a better understanding of its petrophysics and thermochemical structure.

In this paper, we present an assessment of the thermoelastic parameters [in the form of P–V–T–K Equations of State (EoS)] of orthopyroxene, clinopyroxene, spinel and garnet based on X-Ray diffraction data and direct elastic measurements available in literature. The newly developed EoS are appropriate to describe the elastic behaviour of these phases under the most relevant P–T conditions and bulk compositions of the Earth's mantle. In combination with the published EoS for mantle olivine and magnesiochromite, these EoS are suitable to calculate the physical properties of mantle peridotites and their variation with P and T.

Thanks to these EoS, we can evaluate how the variations in bulk composition and thermal regimes affect the density structure of the lithospheric mantle. Accordingly, the density structure of fertile and depleted peridotitic systems was calculated along the 35, 45 and 60 mWm^{-2} geothermal gradients at P comprised between 1 and 8 GPa. Under very cold geothermal gradients, the density of both fertile and depleted peridotitic systems progressively increases with depth, whereas under relatively hot conditions a first downwards decrease from 1 to ca 3 GPa is observed, followed by an increase downward. In mantle sections characterized by intermediate geotherms (45 mWm^{-2}), the behaviour of the two systems differs up to ca 4 GPa, as the density of the depleted system remains nearly constant down to this depth whereas it moderately increases in the fertile system.

The results of our simplified parameterisation, in agreement with classical thermodynamic modelling, indicate that the density structure of the lithospheric mantle is predominantly controlled by the P – T gradient variations, with some compositional control mostly arising at cold-intermediate thermal conditions. Integrated by geophysical and thermodynamic modelling, the newly developed and selected EoS could provide an alternative strategy to infer the elastic properties of mineral phases and peridotite rocks, under the most relevant P–T conditions and compositions of the Earth's mantle, without requiring sets of end-member properties and solution models.

Keywords: Equations of State, Mantle minerals, Upper mantle density structure, Fertile and depleted peridotites, Cold-hot geotherms

1. Introduction

Understanding the density structure of the upper mantle is critical to our comprehension of the tectonic and magmatic evolution of the lithosphere (e.g., Braun, 2010; Capitanio et al., 2007; Simon and Podladchikov, 2008; Thybo and Artemieva, 2013) and crucial to address complex geodynamic phaenomena (e.g., mantle convection, plume upwelling, slab subduction, crustal movements). The density of the upper mantle ultimately depends on both its thermal and compositional structure, which

55 can be derived from petrological-geochemical studies on exhumed mantle samples, i.e., xenoliths and
56 tectonically exposed mantle sections, and from the interpretation of seismic data (and in general of
57 geophysical observables, e.g., gravity anomalies, surface heat flow, etc.).
58 Thermobarometric, petrochemical and isotopic studies of xenoliths and exposed mantle sections can
59 help in unveiling the compositional and thermal structure of their source mantle at the time of the
60 eruption or emplacement (e.g., Coltorti et al., 2021; Mazzucchelli et al., 2009; Melchiorre et al., 2020;
61 Pearson et al., 2003) but the structure of the lithosphere may only be defined at a local scale, as large
62 portions remain inaccessible. Differently, seismic data are endowed with a more continuous spatial
63 coverage, to such an extent that the mantle may be imaged at a lithospheric scale; however, their
64 conversion into models of the upper mantle is not straightforward (Afonso et al., 2013, and references
65 therein). The interpretation of seismic data relies on appropriate combinations of the observed seismic
66 wave velocities with either thermodynamic concepts and/or experimental data from mineral physics
67 (e.g., Bass and Anderson, 1984) and needs to account for both compositional and thermal signatures
68 in wave velocities. Uncertainties in data interpretation are further exacerbated since ultramafic rocks
69 with different compositions can fit equally well wave velocities (e.g., Afonso et al., 2013).
70 In general, addressing the thermochemical structure of the mantle requires the calculation of mineral
71 and rock physical properties (elastic *moduli*, thermal expansions, densities, etc.) at elevated pressure
72 and temperature. Unequivocally, the knowledge of accurate elastic parameters of candidate mantle
73 phases, and their variations with pressure and temperature, is required. In this context, the Equations
74 of State (EoS) of mantle phases are undoubtedly the best proxy for unravelling the structure and
75 dynamics of the Earth's mantle (e.g., Afonso et al., 2007; Stixrude and Lithgow-Bertelloni, 2005a)
76 and its evolution through time, as they can define how volume, density or the elastic properties of
77 minerals vary with pressure and/or temperature (e.g., Angel, 2000). For rocks, the elastic properties
78 have to be inferred from those of their constituent minerals, at appropriate conditions (Connolly,
79 2009). This is commonly done by phase equilibria calculations based on thermodynamic data (Afonso
80 et al., 2008; Connolly and Petrini, 2002; Stixrude and Lithgow-Bertelloni, 2011, 2005b) (see

Connolly, 2009 for extensive considerations of phase equilibria calculations to geodynamic modelling), with aggregate properties calculated by any standard solid mixing theory (e.g., Abers and Hacker, 2016; Hacker and Abers, 2004, and references therein). As mass in aggregates is a simple sum of chemical component masses, the density of rocks can be then calculated from the density of constituent minerals according to their volume proportion.

Several studies ~~have~~ attempted to evaluate the density distribution of the lithosphere, ~~which is~~ known to be vertically and laterally heterogeneous due to variable mineralogy (in terms of mineral and modal compositions), complex phase transitions and differing thermal regimes. It was showed that the increase of Mg/(Mg+Fe) during partial melting lowers the bulk density of the mantle (Schutt and Lesher 2006), but is not affecting phase transitions unlike Na content, which controls the spinel – plagioclase transition and may play an important role in areas of high heat flows and thin crust (Simon and Podladchikov, 2008). Further studies investigated the density structure of mantle sections either by combining data from petrology, mineral physics and geophysics (e.g., Fullea et al., 2014) or by classic thermodynamic calculations complemented for the most relevant Cr-bearing phases in the upper mantle (Ziberna and Klemme, 2016). These studies showed some contrasting results as to whether the predominant control on the density variations of the lithosphere is due to the thermal state, bulk composition, or their interplay.

In this work, we set out to explore the density structure of the lithospheric mantle, and its variation with changes in bulk composition and thermal gradient, from the perspective of the EoS of its constituent minerals, following a simplified parameterisation. The first part presents an assessment of the thermoelastic parameters of orthopyroxene, clinopyroxene, spinel and garnet. To this aim, pre-existing literature data on compressibility, thermal expansion and elasticity of these phases were used to constrain their P–V–T–K (P = pressure, V = volume, T = temperature, K = bulk modulus) EoS in peridotitic systems (i.e., preferentially selecting data measured on crystals with chemical compositions comparable to those expected in the upper mantle). As already computed in recent detailed studies, P–V–T–K and P–V–T EoS for mantle olivine and magnesiochromite were selected

from literature (Angel et al., 2018; Nestola et al., 2019); two distinct EoS were used for mantle spinels to account for the variation of their elastic properties in response to varying Cr and Al contents (cfr. Section 2.3). The second part of this work aims at investigating how the density structure of fertile and depleted lithospheric mantle sections is affected by different thermal regimes (35, 45 and 60 mWm^{-2} geothermal gradients), following a simplified parameterisation that does not incorporate phase relations. Beyond exploring the density variations with this approach, we also provide a comparison with classic thermodynamic modelling (Perple_X; Ziberna and Klemme, 2016). This comparison allowed to assess that (i) the density profiles can be readily computed following our simplified parameterisation, (ii) the thermal gradient is the controlling variable when it comes to the density structure of the lithosphere and (iii) the newly developed and selected EoS consistently describe the elastic behaviour of the related phases under the most relevant P–T conditions and compositions of the Earth's mantle, without requiring sets of end-member properties and solution models.

2. Data selection and EoS fitting

There are two possible approaches to describe the P–V–T or P–V–T–K behaviour of solids: thermal-pressure models (Holland-Powell and Mie-Grüneisen-Debye thermal‑pressure EoS) and isothermal-type models at high temperature (cfr. Angel et al., 2018). For extensive considerations to these issues the reader is referred to Anderson (1995), Angel (2000) and Angel et al. (2018).

The thermoelastic properties for mantle olivine (Fo_{90-92}) have been extensively reviewed and the P–V–T–K EoS was recently published (Angel et al., 2018). Considering the P – T ranges of our investigation, we selected the third-order Birch-Murnaghan compressional EoS in combination with the isothermal-type model for all the computations.

The P–V–T EoS for mantle magnesiochromite was also recently published (Nestola et al., 2019), parametrised as second-order Birch-Murnaghan compressional EoS in combination with the Holland-Powell thermal‑pressure EoS; this formulation was used for the computations of magnesiochromite

for the depleted peridotitic system. The selected thermoelastic parameters for mantle olivine and mantle magnesiochromite are reported in Table 1.

The thermoelastic behaviour of pyroxenes, spinel and garnet was here constrained based on X-Ray diffraction data (compressibility and thermal expansion) and elasticity measurements available in literature. The full EoS for these phases were solved with the EosFit7c program (Angel et al., 2014) following the approach of Milani et al. (2017) to perform simultaneous fits of elastic moduli and cell parameters. For every phase, each individual data set of volumes was scaled to its own volume at room conditions prior to fitting the data together. Additionally, in order to compare X-Ray diffraction and elasticity measurements, K_{SR} (adiabatic Reuss bulk moduli, from elasticity data) were converted into K_{TR} (isothermal Reuss bulk moduli, from X-Ray diffraction data) according to the relationship $K_{SR} = (1 + \alpha_V \gamma T) K_{TR}$ where α_V is the volume thermal expansion (taken from the EoS itself, at the P – T of interest) and γ is the Grüneisen parameter (taken from literature).

2.1 Orthopyroxene

Mantle orthopyroxenes (space group *Pbca*) are solid solutions between enstatite ($Mg_2Si_2O_6$) and ferrosilite ($Fe_2Si_2O_6$) end-members and typically contain few wt% of Al_2O_3 and some CaO as well (e.g., McDonough and Rudnick, 1998). A reanalysis of K_{TR} and its pressure derivative K'_{TR} of $Mg_2Si_2O_6$ based on different experiments (two compression, one Brillouin measurement and one ultrasonic measurement) (Angel and Jackson, 2002) yielded the best estimates of $K_{TR,0}$ and $K'_{TR,0}$, being respectively 105.8(5) GPa and 8.5(3). By comparison, measurements on aluminium-bearing natural orthopyroxenes showed higher bulk moduli and lower pressure derivatives (Chai et al., 1997; Hugh-Jones et al., 1997; Zhang and Bass, 2016, refit of their data) than that of $Mg_2Si_2O_6$. For these reasons, $Mg_2Si_2O_6$ enstatite cannot be considered a good representation of the elastic behaviour of the orthopyroxene component in the lithospheric upper mantle.

We selected data from five different experiments on mantle orthopyroxenes: two compressions (Hugh-Jones and Angel, 1997) [samples *N1* and *N2*]), two expansions (Yang and Ghose, 1994

158 [sample *Fs20*]; Scandolo et al., 2015 [sample *B22 N.60*]) and one high-pressure Brillouin
159 measurement (Zhang and Bass, 2016). We are not aware of any volume measurements on either
160 mantle-composition orthopyroxene or enstatite made at low temperature; consequently, the Einstein
161 temperature (θ_E) could not be refined and was fixed at 510 K (Holland and Powell, 2011,
162 corresponding to Fs20). The Grüneisen parameter (0.85, for Fs20) was taken from Yang and Ghose
163 (1994) and assumed that it does not vary with temperature. With these constraints, we fitted
164 simultaneously each individual data set with a third-order Birch-Murnaghan compressional EoS in
165 combination with the isothermal-type model (parameterisation from Angel et al., 2018); the final
166 refined EoS parameters (Table 1) fit all the data within the experimental uncertainties (Supplementary
167 Material File 1, Figure S1). The final EoS for mantle orthopyroxene is provided in Supplementary
168 Material File 2.
169
170 **2.2 Clinopyroxene**
171 Mantle clinopyroxenes (space group *C2/c*) are solid solutions between diopside ($CaMgSi_2O_6$) and
172 hedenbergite ($CaFeSi_2O_6$) end-members and typically contain few wt% of Al_2O_3, some Cr_2O_3 as well
173 as Na_2O (e.g., McDonough and Rudnick, 1998).
174 A survey of the literature showed that $K_{TR,0}$ and $K'_{TR,0}$ values for $CaMgSi_2O_6$ diopside and near end-
175 member compositions exhibit large variations; the same is for $K_{S,0}$ and $K'_{S,0}$ (see Xu et al., 2019 for a
176 recent compilation of literature data).
177 We selected data from six different experiments on diopside and near end-member compositions: one
178 compression (Li and Neuville, 2010 [room temperature data]), three expansions (Cameron et al., 1973
179 [sample *Diopside*]; Pandolfo et al., 2015 [sample *Di*]; Prencipe et al., 2000), one high-pressure
180 Brillouin measurement (Sang and Bass, 2014) and one high-temperature RUS measurement (Isaak et
181 al., 2006). The Grüneisen parameter (0.867) is taken from Isaak et al. (2006) and assumed that it does
182 not vary with temperature. $K_{SR,0}$ for near end-member diopsides recalculated from C_{ij} data of Sang
183 and Bass (2014) and Isaak et al. (2006) are significantly different between each other (respectively,

111.2(7) GPa vs 113.4(9) GPa). To make the fit consistent between these two data sets, we excluded $K_{SR,0}$ of Sang and Bass (2014). We also excluded from the fit the data point of Sang and Bass (2014) at 14 GPa, which lies completely outside the trend (Supplementary Material File 1, Figure S2). With these constraints, we fitted simultaneously each individual data set with a third-order Birch-Murnaghan compressional EoS in combination with the isothermal-type model (parameterisation from Angel et al., 2018); the final refined EoS parameters (Table 1) fit almost all the data within the experimental uncertainties (Supplementary Material File 1, Figure S2). The final EoS for mantle clinopyroxene is provided in Supplementary Material File 3.

Bearing in mind that the selected data sets correspond to near end-member and $CaMgSi_2O_6$ diopside, it must be considered carefully whether the final refined thermoelastic parameters are a good representation of the elastic behaviour of the clinopyroxene component in the lithospheric upper mantle. Indeed, clinopyroxenes with augitic compositions are a common species occurring in a wide variety of igneous rocks and can be occasionally found in ultrabasic rocks. Xu et al. (2017) and (2019) recently studied the thermoelastic behaviour of augite by synchrotron-based X-Ray diffraction combined with an externally heated diamond anvil cell. Their experiments yielded respectively $K_{TR,0}$ = 111(1) GPa, $K'_{TR,0}$ = 4.1(1) and $K_{TR,0}$ = 112(3) GPa, $K'_{TR,0}$ = 5.0(7). These results prove that clinopyroxenes with augitic compositions behave similarly to near end-member diopsides. Therefore, we are confident that our P–V–T–K EoS parameters can be applied to a wide range of mantle clinopyroxene compositions.

2.3 Spinel

Mantle spinels (space group *Fd-3m*) show extensive solid solution between end-members as they typically vary in composition between four components: spinel s.s. ($MgAl_2O_4$), hercynite ($FeAl_2O_4$), magnesiochromite ($MgCr_2O_4$) and chromite ($FeCr_2O_4$). The compositional variations in mantle spinels are mainly displayed in their Cr/(Cr + Al) and Mg/(Mg + Fe) molar ratios, which reflect the degree of melt depletion experienced by a peridotite. Indeed, spinels with high Al and low Cr contents

characterize lherzolites, whereas low Al and high Cr contents distinguish harzburgitic spinels (e.g., McDonough and Rudnick, 1998).

The bulk modulus systematics for Mg-Fe-Cr-Al spinels have been recently analysed by Nestola et al. (2015, and references therein), who showed that: (i) the Cr-Al substitution considerably changes the $K_{TR,0}$ [192(1) vs 182.5(1.4) GPa for $MgAl_2O_4$ and $MgCr_2O_4$, respectively]; (ii) the Fe-Mg substitution does not substantially affect the bulk modulus for either Cr or Al spinels [193.9(1.7) vs 184.8(1.7) GPa for $FeAl_2O_4$ and $FeCr_2O_4$, respectively], with the $K'_{TR,0}$ similar for all four end-members. Thus, the $K_{TR,0}$ of Mg-Fe-Cr-Al spinels is roughly controlled by the Cr/Al ratio. Hence, two EoS are needed to properly describe the elastic behaviour of mantle spinels: one EoS for lherzolitic spinels and another EoS (selected from Nestola et al., 2019, see above) for harzburgitic spinels (magnesiochromites).

To constrain the elastic behaviour of Al-rich lherzolitic spinels, we selected data from six different experiments: one compression (Nestola et al., 2007 [sample *disordered*]), three expansions (Carbonin et al., 2002 [sample *NAT*]; Grimes and Al-Ajaj, 1992; Martignago et al., 2003 [sample *H-Cr*]), one high-pressure Brillouin measurement (Speziale et al., 2016) and one high-temperature RPR measurement (Suzuki et al., 2000). The Grüneisen parameter (1.17) was taken from Suzuki et al. (2000) and assumed that it does not vary with temperature. Because the quoted uncertainties of K_{SR} from Suzuki et al. (2000) are substantially smaller than those expected from elasticity measurements (e.g. 1 to 3 GPa), we under-weighted the experimental data (1% esd was assumed for all data). With these constraints, we fitted simultaneously each individual data set with a third-order Birch-Murnaghan compressional EoS in combination with the Holland-Powell thermal-pressure EoS; the final refined EoS parameters (Table 1) fit almost all the data within the experimental uncertainties (Supplementary Material File 1, Figure S3). The final EoS for mantle spinel is provided in Supplementary Material File 4. Considering the bulk modulus systematics for Mg-Fe-Cr-Al spinels, we are confident that our P–V–T–K EoS parameters can be applied to a wide range of Al-rich spinel compositions.

236

237 **2.4 Garnet**

238 Mantle garnets (space group *Ia-3d*, general formula $X_3Y_2Si_3O_{12}$) are multicomponent substitutional
239 solid solutions since different cations can be mutually exchanged at the X (Mg, Fe, Ca, Mn divalent
240 cations) and Y (Al, Fe, Cr trivalent cations) sites. Compositionally, the most significant components
241 of peridotitic garnets are $Mg_3Al_2Si_3O_{12}$ pyrope (ca 75%), $Ca_3Al_2Si_3O_{12}$ grossular (ca 10%) and
242 $Fe_3Al_2Si_3O_{12}$ almandine (ca 15%) (e.g., Wood et al., 2013).

243 The effect of Mg-Fe substitution for the pyrope-almandine solid solution was recently analysed by
244 Lu et al. (2013) and Milani et al. (2015). Milani et al. (2015) determined $K_{TR,0}$ = 163.7(1.7) GPa for
245 pyrope, $K_{TR,0}$ = 167.2(1.7) GPa for an intermediate $Py_{60}Alm_{40}$ and $K_{TR,0}$ = 172.6(1.5) GPa for
246 almandine, with similar $K'_{TR,0}$ for all three garnets, claiming that Fe substituting for Mg linearly
247 increases $K_{TR,0}$ but does not affect $K'_{TR,0}$. However, compared to the sources reviewed by Milani et
248 al. (2015), the determined $K_{TR,0}$ values are notably lower than expected whereas $K'_{TR,0}$ are slightly
249 higher and this can be ascribed to the well-known trade-off between fit values for $K_{TR,0}$ and $K'_{TR,0}$. Lu
250 et al. (2013) measured the elasticity of a Fe-bearing pyrope by high P-T Brillouin spectroscopy,
251 determining $K_{SR,0}$ = 168.2(1.8) and $K'_{SR,0}$ = 4.4(1). Comparative analysis of these results led the
252 authors to conclude that addition of Fe does significantly affect $K_{SR,0}$ but rather has a weak positive
253 effect on $K'_{SR,0}$. A similar conclusion was reached by Jiang et al. (2004), who showed that Fe
254 substituting for Mg in the pyrope-almandine series has a little effect on the bulk modulus (almandine
255 $K_{SR,0}$ being 2% higher than that of pyrope) while it increases its pressure derivative. The effect of Ca-
256 Mg substitution for the pyrope-grossular solid solution has been analysed again by Jiang et al. (2004),
257 who showed that the $K_{SR,0}$ varies by ca 2% across the pyrope-grossular system and that there are no
258 evident trends in the $K'_{SR,0}$. In view of these considerations, we selected data from four different
259 experiments: one compression (Milani et al., 2015 [sample $Py_{60}Alm_{40}$]), two expansions (Bosenick
260 and Geiger, 1997 [excluding the scattered data at 220 K], Milani et al., 2015 [sample Py_{100}]) and one
261 high-temperature RUS measurement (Suzuki and Anderson, 1983). The Grüneisen parameter (1.19)

was taken from Gillet et al. (1992) and assumed that it does not vary with temperature. With these constraints, we fitted simultaneously each individual data set with a third-order Birch-Murnaghan compressional EoS in combination with the Holland-Powell thermal-pressure EoS; the final refined EoS parameters (Table 1) fit all the data within the experimental uncertainties (Supplementary Material File 1, Figure S4). The final EoS for mantle garnet is provided in Supplementary Material File 5. Considering the bulk modulus systematics for Mg-Fe-Ca aluminous garnets, we are confident that our P–V–T–K EoS parameters can be applied to a wide range of mantle garnet compositions.

3. Density variations in the lithospheric mantle

3.1 Density calculations

The density of mantle peridotites is function of the chemical composition, modal abundance and elastic properties of their constituent minerals, which in turn are controlled by pressure, temperature and bulk composition of the system. Here, the density structure of the lithospheric mantle was calculated following a two-step approach.

The first step involved the calculation of density profiles for each phase along the geothermal gradients of interest. To our purposes, three geothermal gradients of 35, 45 and 60 mWm^{-2} were chosen as considered representative of extremely cold, intermediate, and relatively hot lithospheric sections. The density of each phase was calculated in the form of 'crystallographic density' according to the relation:

$$\rho_{(phase\ at\ PT)} = \frac{Z_{(phase)} \times Mw_{(phase)}}{\left(\frac{V}{V0}\right)_{(EoS\ at\ PT)} \times V0_{(phase)} \times Na} \qquad (1)$$

where $\left(\frac{V}{V0}\right)_{(EoS\ at\ PT)}$ represents the volume [here the normalized volume $\left(\frac{V}{V0}\right)$] calculated from the EoS at specific P – T conditions (e.g., for a characteristic geotherm or at any P – T), $V0_{(phase)}$ is the reference unit cell volume of the phase measured at ambient conditions, $Mw_{(phase)}$ its molecular weight, $Z_{(phase)}$ is the number of formula units in the unit cell and Na the Avogadro number.

285 The second step involved the calculation of density profiles for bulk rocks, which were here
286 calculated from the densities ρ_i of n constituent minerals as:

287 $$\rho_{(bulk\ rock)} = \left(\sum_{i=1}^{n} \rho_i \times v_i\right)/n \qquad (2)$$

288 where v_i is the volume proportion of each mineral.

289 We computed density profiles for all constituent mineral phases and for two potential lithospheric
290 mantle sections, a fertile and a depleted peridotitic systems, along the 35, 45 and 60 mWm^{-2}
291 geothermal gradients. Calculations for the two lithospheric sections were restricted to a P – T range
292 of 1 – 8 GPa and 350 – 1375 °C. These gradients were selected from the preferred geotherm family
293 of Hasterok and Chapman (2011), which are based on radiogenic heat production measurements
294 together with xenolith thermobarometry and tectonothermal constraints. Following Hasterok and
295 Chapman (2011), we assumed that the transition from a conductive to an adiabatic geotherm
296 corresponds to the lithosphere-asthenosphere boundary (LAB), which is here used only to discuss the
297 effect of temperature on density profiles.

298 Our calculations at subsolidus conditions do not include the effects of porosity, mineral texture and
299 rock microstructure as well as no volatile-bearing phases, thus excluding OH groups in NAMs and/or
300 intergranular fluids and/or melts.

301 Calculations were based on previously studied natural peridotite xenoliths: a spinel lherzolite from
302 the Veneto Volcanic Province (sample SG34 from Beccaluva et al., 2001) was adopted as
303 representative of a fertile mantle, while a spinel harzburgite from Grande Comore island (sample
304 NDR13, unpublished data from Coltorti et al., 1999), now under investigation for other petrological
305 studies, was chosen to represent a depleted mantle. Modal compositions of the selected samples were
306 calculated by least-squares mass balance using bulk-rock and mineral major element analyses (Tables
307 2, 3).

308 Bearing in mind that calculating the density of each phase requires a reference unit cell volume
309 measured at ambient conditions ($V0_{(phase)}$, equation 1), olivine, pyroxenes, spinel and garnet unit

cell parameters (and related crystal chemical compositions, which slightly differ compared to those expected from our models of fertile and depleted mantle) were selected from literature (Tables 2, 3). Modal compositions were kept from the two selected mantle xenoliths (SG34 spinel lherzolite and NDR13 spinel harzburgite), however density calculations were carried out by using the mineral compositions and unit cell volumes of the reference minerals from the literature. All selected mineral compositions were kept fixed for all density calculations.

The spinel-garnet transition was modelled according to the approximate reaction spinel + pyroxenes = garnet + olivine (e.g., Klemme and O'Neill, 2000); mineral modes in the garnet stability field were calculated from stoichiometric balance upon completion of the reaction (Tables 2, 3). Recent thermodynamic modelling in natural peridotitic systems (Ziberna et al., 2013) indicates that garnet and spinel always coexist and the width and depth of the coexistence interval strongly, but not only, depends on the thermal state of the lithosphere (restricted depth interval - about 15 km - in regions with hot geotherms, and much broader interval - over 100 km - for cold geotherms). We simplified this model by assuming garnet + spinel coexistence intervals of 1.5 – 4 GPa, 1.5 – 3 GPa and 1.8 – 2.4 GPa along the 35, 45 and 60 mWm^{-2} geothermal gradients, respectively, for both fertile and depleted mantle sections. For density calculations, mineral modes were kept fixed in spinel and garnet stability fields, and were imposed to vary linearly in the spinel-garnet stability field.

3.2 Results

Density profiles for both mineral phases and the fertile and depleted peridotitic systems were calculated along three different geothermal gradients: 35 mWm^{-2} (Figures 1, 2), representative of the coldest cratonic mantle sections, 45 mWm^{-2} (Figures 1, 3), typical of average cratonic sections, and 60 mWm^{-2} (Figures 1, 4), for relatively hot, off-craton, lithospheric sections (Hasterok and Chapman, 2011).

Figure 1 shows that, despite mineral phases having different elastic parameters (Table 1), their density variation with depth is largely controlled by the geothermal gradients. Under cold conditions (35

336 mWm^{-2}), density curves for all phases shows a subtle but significant decrease down to ca 1 GPa,
337 which is followed by a marked increase for olivine and pyroxenes and a moderate increase for spinel,
338 magnesiochromite and garnet. Under relatively hot conditions (60 mWm^{-2}), density curves for all
339 phases exhibit a marked decrease down to ca 3 GPa, followed by an increase with depth. It is under
340 intermediate conditions (45 mWm^{-2}) and at P > 1 GPa that density curves exhibit most of the
341 differences. Indeed, density curves for all mineral phases show a gentle decrease down to ca 1 GPa,
342 where the density of olivine and pyroxenes starts to increase, whereas it continues to decrease down
343 to ca 4.5 GPa for spinel, magnesiochromite and garnet. Such distinct behaviour is clearly due to
344 different elastic parameters (Table 1), but it is also due to the interplay between increasing
345 temperature and pressure, whose effects are of the same order (see also considerations below).
346 Noteworthy errors associated with density calculations through the newly developed and two selected
347 EoS are minimum (Figure 1), and this in turn affects the accuracy of density profiles for bulk rocks.
348 Such errors, esd($\rho/\rho 0$) ~ 10^{-3}, translate to uncertainties of density calculations which are ~ 0.05 %
349 (e.g., 3.416(2) g/cm^3 or conversely 3416(2) kg/m^3 at ~ 6 GPa and ~1050 °C for the fertile peridotitic
350 system), which are considerably much less than average uncertainties associated to density
351 calculations.
352 If we consider a geotherm of 35 mWm^{-2} and both fertile and depleted compositions (Figure 2), the
353 density in the mantle shows a similar behaviour, progressively increasing with increasing depth. This
354 indicates that the effect of pressure prevails over that of the slowly rising temperature. By comparing
355 the trends of the fertile and depleted mantle sections (Figure 5), it is evident that the former is typified
356 by a more pronounced density increase with respect to the depleted one. This is attributable to the
357 higher modes of garnet (due to higher bulk Al_2O_3 in fertile compositions), which is among the densest
358 mineral phases in peridotite assemblages (e.g., Lee, 2003).
359 If we consider a geotherm of 45 mWm^{-2}, results are somehow different in the 1-4 GPa interval. Here,
360 the density of the depleted peridotitic system remains nearly constant while it moderately increases
361 for the fertile system; then the density of both systems increases from 4 down to 8 GPa (Figures 3,

5). These results suggest that (i) the effect of temperature on the evolution of the bulk density with depth is comparable to that of pressure and that (ii) the behaviour of the two systems is decoupled down to ca 4 GPa.

If we consider a relatively hot geotherm of 60 mWm^{-2}, the temperature increase with depth is so strong that leads to an overall decrease of the bulk density of both depleted and fertile systems in the lithosphere from 1 to about 3 GPa, followed by an increase from 3 down to 8 GPa (Figure 4). By comparing the trends of the two sections (Figure 5), the fertile system shows a more gentle decrease in its density compared to the depleted system. This is again attributable to the higher modes of garnet, which, combined with the P – T gradient effects, result in a slightly smoother density profile. Irrespective of the specific depth and width of their coexistence intervals, spinel and garnet have a stronger control on the density variations in case of fertile compositions, due to their higher modes.

3.3 Discussion

3.3.1 Density models and the effect of the thermal state

Most of the recently published upper mantle density models derive from phase equilibria calculations based on thermodynamic data, where stable mineral assemblages are computed using Gibbs free-energy minimization techniques. Previous works (Fullea et al., 2014; Ziberna and Klemme, 2016) showed some contrasting results as to whether the lithospheric density is predominantly controlled by the thermal state, bulk composition, or their interplay. Fullea et al. (2014) unravelled the present-day Irish lithospheric structure through LitMod3D code (Fullea et al., 2009) that combines petrological and geophysical observations with thermodynamic data (in the CFMAS system) within a self-consistent framework. This modelling revealed similar vertical density profiles - sharp spinel – garnet phase transition with an abrupt increase of density, a general trend of decreasing density down to ~ 100 km, followed by an increase (Figure 5) - associated with all the mantle compositions discussed in the work (i.e., from fertile to moderately depleted peridotites). Overall, these density trends suggest a greater control of the thermal state on the lithospheric density rather than bulk

388 composition in the Irish lithosphere (60 to 70 mWm^{-2}). Considering the lack of Cr (for which there is
389 evidence that it may considerably change phase relations in the upper mantle) in most previous
390 calculations, Ziberna and Klemme (2016) investigated the density variations for Cr-bearing mantle
391 compositions (Pali-Aike xenoliths, Patagonia) in response to changes in bulk compositions and
392 thermal gradients by means of well-established free energy minimization techniques, with
393 thermodynamic calculations based on the internally consistent dataset of Holland and Powell (1998)
394 complemented for the most relevant Cr-bearing phases in the upper mantle (Ziberna et al., 2013).
395 Contrary to previous results (Fullea et al., 2014), this work showed that the density profiles across
396 the spinel – garnet peridotite transition are not sharp and depend both on bulk composition (especially
397 on Al_2O_3 and Cr_2O_3) and geothermal gradient (Figure 5). Moreover, while under relatively hot
398 thermal conditions (70 mWm^{-2}) density profiles for both fertile and depleted compositions show
399 similar trends (i.e., density decrease down to ca 2.5 GPa), this is not the case for intermediate thermal
400 conditions (50 mWm^{-2}) where density in the mantle for depleted compositions remains virtually
401 constant down to ca 4 GPa and it rapidly increases for more fertile compositions (Figure 5).
402 Accordingly, these authors suggested that it is the interplay between bulk composition and thermal
403 gradient that controls density variations in the lithospheric mantle.
404 Our models predict a much greater thermal control over the density of the lithospheric mantle, with
405 some compositional control mostly arising at cold-intermediate thermal conditions (Figure 5).
406 Considering that we based the spinel – garnet phase transitions on Ziberna et al. (2013)
407 thermodynamic model (cfr. ~~Density calculations section~~ Section 3.1), spinel and garnet coexist over
408 a significant depth interval. Accordingly, our models predict a smooth variation of densities across
409 the spinel – garnet transition and no abrupt changes. As already evidenced by Ziberna and Klemme
410 (2016), the sharp spinel – garnet transitions associated with an abrupt change of density identified by
411 Fullea et al. (2014) can be ascribed to the lack of Cr in their thermodynamic model. If this aspect is
412 ruled out from further discussion, and density curves are analysed overall, there are some similarities
413 with those from Fullea et al. (2014) (Figure 5). Indeed, all modelled compositions exhibit an overall

414 decrease of the bulk density up to about 100 km, followed by an increase downwards, for relatively
415 hot thermal conditions (60 to 70 mWm^{-2}). Our density curves show even more striking similarities
416 with those from Ziberna and Klemme (2016), for which a similar behaviour is predicted for fertile
417 and depleted compositions under relatively hot thermal conditions (70 mWm^{-2}), and a different one
418 under intermediate conditions (50 mWm^{-2}) (Figure 5). Therefore, our investigation shows that density
419 profiles in natural systems with simplified phase relations display comparable trends to those reported
420 in previous studies. In this framework, perspectives are that the thermal gradient exerts substantial
421 control when it comes to the density structure of the lithosphere and that the compositional control
422 on the density evolution with depth may be less than previously suggested. In the next section, we
423 show how density calculations based on simplified phase relations can be reconciled with Perple_X-
424 based results from previous literature. We also infer the thermal gradient is the main controlling
425 variable of the lithospheric mantle density.
426
427 **3.3.2 Comparison between Perple_X and simplified calculations**
428 Although a strict evaluation of similarities and differences of our simplified parameterisation for
429 calculating density variations with respect to classic thermodynamic modelling (e.g., Perple_X) goes
430 beyond the scope of this paper (detailed results of the application of both models to a real mantle
431 section will be presented elsewhere), in the following we provide an application of our model
432 compared with previous results from literature (Ziberna and Klemme, 2016). To this aim, we selected
433 two of the four representative mantle xenoliths from Pali-Aike, Patagonia, reported in Ziberna and
434 Klemme (2016), namely PA3 (spinel harzburgite) and BN4 (spinel-garnet lherzolite), for which we
435 computed density profiles along the 50 and 70 mWm^{-2} geothermal gradients (Figure 6). Input data
436 for Ziberna and Klemme (2016) thermodynamic modelling are whole-rock analyses from Stern et al.
437 (1999), with calculations performed in the SiO_2-Al_2O_3-Cr_2O_3-FeO-MgO-CaO-Na_2O system. In order
438 to provide a clear and consistent comparison between the two methods, input data (i.e., mineral

compositions and modes) for our simplified parameterisation were as follows. Olivine, pyroxenes, and spinel mineral compositions and modes were selected from Perple_X calculations of Ziberna and Klemme (2016) at 1 GPa (at the corresponding temperature for the 50 and 70 mWm^{-2} geothermal gradients). Garnet compositions were selected from Perple_X calculations of Ziberna and Klemme (2016) at P – T corresponding to spinel-out reaction (which depends on bulk composition and geothermal gradient); garnet, as well as olivine and pyroxenes modes in the garnet stability field, were calculated from stoichiometric balance upon completion of the reaction spinel + pyroxenes = garnet + olivine, using the selected mineral modes and compositions. Selected mineral compositions were kept fixed along the whole section; mineral modes were kept fixed in spinel and garnet stability fields, and were imposed to vary linearly in the spinel-garnet stability field (cfr. ~~Density calculations section~~ Section 3.1). Depth intervals of coexistence of spinel + garnet were selected again from Perple_X calculations of Ziberna and Klemme (2016). Density variations with depth and thermal regime for PA3 (spinel harzburgite) and BN4 (spinel-garnet lherzolite) mantle xenoliths are reported in Figure 6, along with original curves from Ziberna and Klemme (2016).

Note that Ziberna and Klemme (2016) thermodynamic model considered phase equilibria, with mineral modes and compositions continuously changing according to P – T conditions, which has not been done in this study. Nonetheless, density curves calculated with our simplified parameterisation match well those from Ziberna and Klemme (2016), both in their general trends with depth and absolute values, with a maximum difference between the two models of ca 20 kg/m^3 (Figure 6). From this similarity, we conclude that our approach with simplified phase relations has enough accuracy for investigating the density structure of the lithosphere. We also infer that the density structure of the lithospheric mantle is predominantly controlled by the thermal gradient variations, with most of the compositional control arising at cold-intermediate thermal conditions. No less importantly, we showed that the newly developed P–V–T–K EoS (pyroxenes, spinel and garnet) in combination with the published EoS for mantle olivine and mantle magnesiochromite are applicable for calculating the

density of mantle peridotites and its variation, with minimum uncertainties, under different thermal regimes and bulk compositions, without requiring sets of end-member properties and solution models.

4. Concluding remarks

In this study, we presented an assessment of the thermoelastic parameters of orthopyroxene, clinopyroxene, spinel and garnet based on X-Ray diffraction data and direct elastic measurements available in literature. The newly developed EoS consistently describe the elastic behaviour of these phases under the most relevant P–T conditions and bulk compositions of the Earth's mantle, along with the published EoS for mantle olivine and magnesiochromite.

As a case study, we evaluated the influence of bulk composition and thermal regimes on the density structure of potential lithospheric mantle sections, following a simplified parameterisation that does not incorporate phase relations. Accordingly, density profiles for fertile and depleted peridotitic systems based on the EoS of their constituent mineral phases were calculated for three different geothermal gradients (35, 45 and 60 mWm^{-2}), for a P – T range of 1 – 8 GPa and 350 – 1375 °C. In case of very cold geotherms (35 mWm^{-2}), the density of both depleted and fertile systems progressively increases with increasing depth. In case of intermediate geotherms (45 mWm^{-2}), the density of a depleted peridotitic system remains nearly constant up to about 4 GPa, while it moderately increases in a fertile system, due to higher modes of garnet. In case of relatively hot geotherms (60 mWm^{-2}), the density of both depleted and fertile systems progressively decreases with increasing depth, up to about 3 GPa, and then increases downwards. Moreover, we also provided an example of application of our model in comparison with classic thermodynamic modelling results from literature. From such comparison, we concluded that (i) density profiles for mantle sections can be computed with enough accuracy following our simplified parameterisation, (ii) the thermal gradient exerts substantial control when it comes to the density structure of the lithosphere and (iii) the compositional control on the density evolution with depth may be less than previously suggested.

Funding

L.F. acknowledges Istituto Nazionale di Geofisica e Vulcanologia (INGV) for funding his Ph.D. project (XXXV cycle) with thematic ‘Links between rheology, mineralogy and composition of the Earth's mantle’ and the Italian National Research Program (PRIN Grant 20178LPCPW ’Micro to Macro - How to unravel the nature of the Large Magmatic Events' to [M.C.])

Acknowledgements

Dr. Luca Ziberna is thanked for providing work files that allowed a validation of our simplified parameterisation for calculating density variations with respect to Perple_X models. The authors are grateful to Michel Grégoire and an anonymous reviewer for their constructive comments, which improved an earlier version of the manuscript. Michael Roden is acknowledged for his careful editorial handling and guidance.

References

Abers, G.A., Hacker, B.R., 2016. A MATLAB toolbox and Excel workbook for calculating the densities, seismic wave speeds, and major element composition of minerals and rocks at pressure and temperature. Geochemistry, Geophys. Geosystems 17, 616–624. https://doi.org/10.1002/2015GC006171

Afonso, J.C., Fernàndez, M., Ranalli, G., Griffin, W.L., Connolly, J.A.D., 2008. Integrated geophysical-petrological modeling of the lithosphere and sublithospheric upper mantle: Methodology and applications. Geochemistry, Geophys. Geosystems 9, Q05008. https://doi.org/10.1029/2007GC001834

Afonso, J.C., Fullea, J., Yang, Y., Connolly, J.A.D., Jones, A.G., 2013. 3-D multi-observable probabilistic inversion for the compositional and thermal structure of the lithosphere and upper mantle. II: General methodology and resolution analysis. J. Geophys. Res. Solid Earth 118,

513 1650–1676. https://doi.org/10.1002/jgrb.50123

514 Afonso, J.C., Ranalli, G., Fernàndez, M., 2007. Density structure and buoyancy of the oceanic
515 lithosphere revisited. Geophys. Res. Lett. 34, 2–6. https://doi.org/10.1029/2007GL029515

516 Anderson, O.L., 1995. Equations of state of solids for geophysics and ceramic science, Oxford
517 Monographs on Geology and Geophysics. https://doi.org/10.1016/0016-7037(95)90195-7

518 Angel, R.J., 2000. Equations of State. Rev. Mineral. Geochemistry 41, 35–59.
519 https://doi.org/10.2138/rmg.2000.41.2

520 Angel, R.J., Alvaro, M., Gonzalez-Platas, J., 2014. EosFit7c and a Fortran module (library) for
521 equation of state calculations. Zeitschrift für Krist. - Cryst. Mater. 229, 405–419.
522 https://doi.org/10.1515/zkri-2013-1711

523 Angel, R.J., Alvaro, M., Nestola, F., 2018. 40 years of mineral elasticity: a critical review and a new
524 parameterisation of equations of state for mantle olivines and diamond inclusions. Phys. Chem.
525 Miner. 45, 95–113. https://doi.org/10.1007/s00269-017-0900-7

526 Angel, R.J., Jackson, J.M., 2002. Elasticity and equation of state of orthoenstatite, MgSiO 3. Am.
527 Mineral. 87, 558–561. https://doi.org/10.2138/am-2002-0419

528 Bass, J.D., Anderson, D.L., 1984. Composition of the upper mantle: Geophysical tests of two
529 petrological models. Geophys. Res. Lett. 11, 229–232.
530 https://doi.org/10.1029/GL011i003p00229

531 Beccaluva, L., Bonadiman, C., Coltorti, M., Salvini, L., Siena, F., 2001. Depletion Events, Nature
532 of Metasomatizing Agent and Timing of Enrichment Processes in Lithospheric Mantle
533 Xenoliths from the Veneto Volcanic Province. J. Petrol. 42, 173–188.
534 https://doi.org/10.1093/petrology/42.1.173

535 Bosenick, A., Geiger, C.A., 1997. Powder X ray diffraction study of synthetic pyrope-grossular

garnets between 20 and 295 K. J. Geophys. Res. Solid Earth 102, 22649–22657. https://doi.org/10.1029/97JB01612

Braun, J., 2010. The many surface expressions of mantle dynamics. Nat. Geosci. 3, 825–833. https://doi.org/10.1038/ngeo1020

Cameron, M., Sueno, S., Prewitt, C.T., Papike, J.J., 1973. High-Temperature crystal chemistry of acmite, diopside, hedenbergite, jadeite, spodumene, and Ureyite. Am. Mineral. 58, 594–618.

Capitanio, F., Morra, G., Goes, S., 2007. Dynamic models of downgoing plate-buoyancy driven subduction: Subduction motions and energy dissipation. Earth Planet. Sci. Lett. 262, 284–297. https://doi.org/10.1016/j.epsl.2007.07.039

Carbonin, S., Martignago, F., Menegazzo, G., Dal Negro, A., 2002. X-ray single-crystal study of spinels: in situ heating. Phys. Chem. Miner. 29, 503–514. https://doi.org/10.1007/s00269-002-0262-6

Chai, M., Brown, J.M., Slutsky, L.J., 1997. The elastic constants of an aluminous orthopyroxene to 12.5 GPa. J. Geophys. Res. Solid Earth 102, 14779–14785. https://doi.org/10.1029/97JB00893

Coltorti, M., Bonadiman, C., Casetta, F., Faccini, B., Giacomoni, P.P., Pelorosso, B., Perinelli, C., 2021. Nature and evolution of the northern Victoria Land lithospheric mantle (Antarctica) as revealed by ultramafic xenoliths. Geol. Soc. London, Mem. 56, M56-2020–11. https://doi.org/10.1144/M56-2020-11

Coltorti, M., Bonadiman, C., Hinton, R.W., Siena, F., Upton, B.G.J., 1999. Carbonatite Metasomatism of the Oceanic Upper Mantle: Evidence from Clinopyroxenes and Glasses in Ultramafic Xenoliths of Grande Comore, Indian Ocean. J. Petrol. 40, 133–165. https://doi.org/10.1093/petroj/40.1.133

Connolly, J.A.D., 2009. The geodynamic equation of state: What and how. Geochemistry, Geophys.

559 Geosystems 10, Q10014. https://doi.org/10.1029/2009GC002540

560 Connolly, J.A.D., Petrini, K., 2002. An automated strategy for calculation of phase diagram sections
561 and retrieval of rock properties as a function of physical conditions. J. Metamorph. Geol. 20,
562 697–708. https://doi.org/10.1046/j.1525-1314.2002.00398.x

563 Fullea, J., Afonso, J.C., Connolly, J.A.D., Fernàndez, M., García-Castellanos, D., Zeyen, H., 2009.
564 LitMod3D: An interactive 3-D software to model the thermal, compositional, density,
565 seismological, and rheological structure of the lithosphere and sublithospheric upper mantle.
566 Geochemistry, Geophys. Geosystems 10. https://doi.org/10.1029/2009GC002391

567 Fullea, J., Muller, M.R., Jones, A.G., Afonso, J.C., 2014. The lithosphere–asthenosphere system
568 beneath Ireland from integrated geophysical–petrological modeling II: 3D thermal and
569 compositional structure. Lithos 189, 49–64. https://doi.org/10.1016/j.lithos.2013.09.014

570 Gillet, P., Fiquetw, G., Malézieux, J.M., Geiger, C.A., 1992. High-pressure and high-temperature
571 Raman spectroscopy of end-member garnets: pyrope, grossular and andradite. Eur. J. Mineral.
572 4, 651–664. https://doi.org/10.1127/ejm/4/4/0651

573 Grimes, N.W., Al-Ajaj, E.A., 1992. Low-temperature thermal expansion of spinel. J. Phys.
574 Condens. Matter 4, 6375–6380. https://doi.org/10.1088/0953-8984/4/30/004

575 Hacker, B.R., Abers, G.A., 2004. Subduction Factory 3: An Excel worksheet and macro for
576 calculating the densities, seismic wave speeds, and H 2 O contents of minerals and rocks at
577 pressure and temperature. Geochemistry, Geophys. Geosystems 5, n/a-n/a.
578 https://doi.org/10.1029/2003GC000614

579 Hasterok, D., Chapman, D.S., 2011. Heat production and geotherms for the continental lithosphere.
580 Earth Planet. Sci. Lett. 307, 59–70. https://doi.org/10.1016/j.epsl.2011.04.034

581 Holland, T.J.B., Powell, R., 2011. An improved and extended internally consistent thermodynamic

582 dataset for phases of petrological interest, involving a new equation of state for solids. J.
583 Metamorph. Geol. 29, 333–383. https://doi.org/10.1111/j.1525-1314.2010.00923.x

584 Holland, T.J.B., Powell, R., 1998. An internally consistent thermodynamic data set for phases of
585 petrological interest. J. Metamorph. Geol. 16, 309–343. https://doi.org/10.1111/j.1525-
586 1314.1998.00140.x

587 Hugh-Jones, D., Chopelas, A., Augel, R., 1997. Tetrahedral compression in (Mg,Fe)SiO 3
588 orthopyroxenes. Phys. Chem. Miner. 24, 301–310. https://doi.org/10.1007/s002690050042

589 Hugh-Jones, D.A., Angel, R.J., 1997. Effect of Ca 2+ and Fe 2+ on the equation of state of MgSiO
590 3 orthopyroxene. J. Geophys. Res. Solid Earth 102, 12333–12340.
591 https://doi.org/10.1029/96JB03485

592 Isaak, D.G., Ohno, I., Lee, P.C., 2006. The elastic constants of monoclinic single-crystal chrome-
593 diopside to 1,300 K. Phys. Chem. Miner. 32, 691–699. https://doi.org/10.1007/s00269-005-
594 0047-9

595 Jiang, F., Speziale, S., Duffy, T.S., 2004. Single-crystal elasticity of grossular- and almandine-rich
596 garnets to 11 GPa by Brillouin scattering. J. Geophys. Res. Solid Earth 109, 1–10.
597 https://doi.org/10.1029/2004JB003081

598 Klemme, S., O'Neill, H.S., 2000. The near-solidus transition from garnet lherzolite to spinel
599 lherzolite. Contrib. to Mineral. Petrol. 138, 237–248. https://doi.org/10.1007/s004100050560

600 Lee, C.-T.A., 2003. Compositional variation of density and seismic velocities in natural peridotites
601 at STP conditions: Implications for seismic imaging of compositional heterogeneities in the
602 upper mantle. J. Geophys. Res. Solid Earth 108, 2441. https://doi.org/10.1029/2003JB002413

603 Li, B., Neuville, D.R., 2010. Elasticity of diopside to 8GPa and 1073K and implications for the
604 upper mantle. Phys. Earth Planet. Inter. 183, 398–403.

https://doi.org/10.1016/j.pepi.2010.08.009

Lu, C., Mao, Z., Lin, J.-F., Zhuravlev, K.K., Tkachev, S.N., Prakapenka, V.B., 2013. Elasticity of single-crystal iron-bearing pyrope up to 20GPa and 750K. Earth Planet. Sci. Lett. 361, 134–142. https://doi.org/10.1016/j.epsl.2012.11.041

Martignago, F., Negro, A.D., Carbonin, S., 2003. How Cr3+ and Fe3+ affect Mg?Al order?disorder transformation at high temperature in natural spinels. Phys. Chem. Miner. 30, 401–408. https://doi.org/10.1007/s00269-003-0336-0

Mazzucchelli, M., Rivalenti, G., Brunelli, D., Zanetti, A., Boari, E., 2009. Formation of Highly Refractory Dunite by Focused Percolation of Pyroxenite-Derived Melt in the Balmuccia Peridotite Massif (Italy). J. Petrol. 50, 1205–1233. https://doi.org/10.1093/petrology/egn053

McDonough, W.F., Rudnick, R.L., 1998. Mineralogy and composition of the upper mantle, in: Reviews in Mineralogy, Vol. 37. pp. 139–164.

Melchiorre, M., Faccini, B., Grégoire, M., Benoit, M., Casetta, F., Coltorti, M., 2020. Melting and metasomatism/refertilisation processes in the Patagonian sub-continental lithospheric mantle: A review. Lithos 354–355, 105324. https://doi.org/10.1016/j.lithos.2019.105324

Milani, S., Angel, R.J., Scandolo, L., Mazzucchelli, M.L., Ballaran, T.B., Klemme, S., Domeneghetti, M.C., Miletich, R., Scheidl, K.S., Derzsi, M., Tokár, K., Prencipe, M., Alvaro, M., Nestola, F., 2017. Thermo-elastic behavior of grossular garnet at high pressures and temperatures. Am. Mineral. 102, 851–859. https://doi.org/10.2138/am-2017-5855

Milani, S., Nestola, F., Alvaro, M., Pasqual, D., Mazzucchelli, M.L., Domeneghetti, M.C., Geiger, C.A., 2015. Diamond–garnet geobarometry: The role of garnet compressibility and expansivity. Lithos 227, 140–147. https://doi.org/10.1016/j.lithos.2015.03.017

Nestola, F., Ballaran, T.B., Balic-Zunic, T., Princivalle, F., Secco, L., Dal Negro, A., 2007.

628 Comparative compressibility and structural behavior of spinel MgAl2O4 at high pressures:
629 The independency on the degree of cation order. Am. Mineral. 92, 1838–1843.
630 https://doi.org/10.2138/am.2007.2573

631 Nestola, F., Periotto, B., Anzolini, C., Andreozzi, G.B., Woodland, A.B., Lenaz, D., Alvaro, M.,
632 Princivalle, F., 2015. Equation of state of hercynite, FeAl2O4, and high-pressure systematics
633 of Mg-Fe-Cr-Al spinels. Mineral. Mag. 79, 285–294.
634 https://doi.org/10.1180/minmag.2015.079.2.07

635 Nestola, F., Zaffiro, G., Mazzucchelli, M.L., Nimis, P., Andreozzi, G.B., Periotto, B., Princivalle,
636 F., Lenaz, D., Secco, L., Pasqualetto, L., Logvinova, A.M., Sobolev, N. V, Lorenzetti, A.,
637 Harris, J.W., 2019. Diamond-inclusion system recording old deep lithosphere conditions at
638 Udachnaya (Siberia). Sci. Rep. 9, 12586. https://doi.org/10.1038/s41598-019-48778-x

639 Pandolfo, F., Cámara, F., Domeneghetti, M.C., Alvaro, M., Nestola, F., Karato, S.-I., Amulele, G.,
640 2015. Volume thermal expansion along the jadeite–diopside join. Phys. Chem. Miner. 42, 1–
641 14. https://doi.org/10.1007/s00269-014-0694-9

642 Pearson, D.G., Canil, D., Shirey, S.B., 2003. Mantle Samples Included in Volcanic Rocks:
643 Xenoliths and Diamonds, in: Treatise on Geochemistry. Elsevier, pp. 171–275.
644 https://doi.org/10.1016/B0-08-043751-6/02005-3

645 Prencipe, M., Tribaudino, M., Pavese, A., Hoser, A., Reehuis, M., 2000. A SINGLE-CRYSTAL
646 NEUTRON-DIFFRACTION INVESTIGATION OF DIOPSIDE AT 10 K. Can. Mineral. 38,
647 183–189. https://doi.org/10.2113/gscanmin.38.1.183

648 Sang, L., Bass, J.D., 2014. Single-crystal elasticity of diopside to 14GPa by Brillouin scattering.
649 Phys. Earth Planet. Inter. 228, 75–79. https://doi.org/10.1016/j.pepi.2013.12.011

650 Scandolo, L., Mazzucchelli, M.L., Alvaro, M., Nestola, F., Pandolfo, F., Domeneghetti, M.C., 2015.
651 Thermal expansion behaviour of orthopyroxenes: the role of the Fe-Mn substitution. Mineral.

652 Mag. 79, 71–87. https://doi.org/10.1180/minmag.2015.079.1.07

653 Schutt, D.L., Lesher, C.E., 2006. Effects of melt depletion on the density and seismic velocity of
654 garnet and spinel lherzolite. J. Geophys. Res. Solid Earth 111.
655 https://doi.org/10.1029/2003JB002950

656 Simon, N.S.C., Podladchikov, Y.Y., 2008. The effect of mantle composition on density in the
657 extending lithosphere. Earth Planet. Sci. Lett. 272, 148–157.
658 https://doi.org/10.1016/j.epsl.2008.04.027

659 Speziale, S., Nestola, F., Jiang, F., Duffy, T.S., 2016. Single-crystal elastic constants of spinel
660 (MgAl2O4) to 11.1 GPa by Brillouin scattering, in: AGU Fall Meeting Abstracts. pp. MR23A-
661 2658.

662 Stern, C.R., Kilian, R., Olker, B., Hauri, E.H., Kurtis Kyser, T., 1999. Evidence from mantle
663 xenoliths for relatively thin (<100 km) continental lithosphere below the Phanerozoic crust of
664 southernmost South America. Lithos 48, 217–235. https://doi.org/10.1016/S0419-
665 0254(99)80013-5

666 Stixrude, L., Lithgow-Bertelloni, C., 2011. Thermodynamics of mantle minerals - II. Phase
667 equilibria. Geophys. J. Int. 184, 1180–1213. https://doi.org/10.1111/j.1365-
668 246X.2010.04890.x

669 Stixrude, L., Lithgow-Bertelloni, C., 2005a. Mineralogy and elasticity of the oceanic upper mantle:
670 Origin of the low-velocity zone. J. Geophys. Res. 110, B03204.
671 https://doi.org/10.1029/2004JB002965

672 Stixrude, L., Lithgow-Bertelloni, C., 2005b. Thermodynamics of mantle minerals - I. Physical
673 properties. Geophys. J. Int. 162, 610–632. https://doi.org/10.1111/j.1365-246X.2005.02642.x

674 Suzuki, I., Anderson, O.L., 1983. Elasticity and thermal expansion of a natural garnet up to 1,000K.

675 J. Phys. Earth 31, 125–138. https://doi.org/10.4294/jpe1952.31.125

676 Suzuki, I., Ohno, I., Anderson, O.L., 2000. Harmonic and anharmonic properties of spinel MgAl 2
677 O 4. Am. Mineral. 85, 304–311. https://doi.org/10.2138/am-2000-2-307

678 Thybo, H., Artemieva, I.M., 2013. Moho and magmatic underplating in continental lithosphere.
679 Tectonophysics 609, 605–619. https://doi.org/10.1016/j.tecto.2013.05.032

680 Wood, B.J., Kiseeva, E.S., Matzen, A.K., 2013. Garnet in the Earth's Mantle. Elements 9, 421–426.
681 https://doi.org/10.2113/gselements.9.6.421

682 Xu, J., Zhang, D., Dera, P., Zhang, B., Fan, D., 2017. Experimental evidence for the survival of
683 augite to transition zone depths, and implications for subduction zone dynamics. Am. Mineral.
684 102, 1516–1524. https://doi.org/10.2138/am-2017-5959

685 Xu, Z., Ma, M., Li, B., Hong, X., 2019. Compressibility and thermal expansion of natural
686 clinopyroxene Di0.66Hd0.13Jd0.12Ts0.05. Results Phys. 12, 447–453.
687 https://doi.org/10.1016/j.rinp.2018.11.077

688 Yang, H., Ghose, S., 1994. Thermal expansion, Debye temperature and Gruneisen parameter of
689 synthetic (Fe, Mg)SiO3 orthopyroxenes. Phys. Chem. Miner. 20, 575–586.
690 https://doi.org/10.1007/BF00211853

691 Zhang, J.S., Bass, J.D., 2016. Single-crystal elasticity of natural Fe-bearing orthoenstatite across a
692 high-pressure phase transition. Geophys. Res. Lett. 43, 8473–8481.
693 https://doi.org/10.1002/2016GL069963

694 Ziberna, L., Klemme, S., 2016. Application of thermodynamic modelling to natural mantle
695 xenoliths: examples of density variations and pressure–temperature evolution of the
696 lithospheric mantle. Contrib. to Mineral. Petrol. 171, 16. https://doi.org/10.1007/s00410-016-
697 1229-9

Ziberna, L., Klemme, S., Nimis, P., 2013. Garnet and spinel in fertile and depleted mantle: insights from thermodynamic modelling. Contrib. to Mineral. Petrol. 166, 411–421. https://doi.org/10.1007/s00410-013-0882-5

Figure captions

Figure 1. Density profiles (ρ/ρ0) for mineral phases in the studied peridotitic systems (olivine, orthopyroxene, clinopyroxene, spinel, magnesiochromite and garnet) calculated along a 35 mWm^{-2} geotherm (blue curves), 45 mWm^{-2} geotherm (yellow curves) and 60 mWm^{-2} geotherm (red curves). The 35, 45 and 60 mWm^{-2} conductive geotherms for density calculations are from Hasterok and Chapman (2011). Esd(ρ/ρ0) (estimated standard deviation) refers to the uncertainties associated with EoS fitting (as calculated by the least-squares method) and density calculations. Note that these uncertainties are minimum.

Figure 2. Density profiles for fertile (left panel) and depleted (right panel) peridotitic systems calculated along a 35 mWm^{-2} geotherm. Brown to yellow colour bar represents the density variations along the profiles. Grey lines subdivide the ideal mantle sections into the spinel, spinel + garnet and garnet stability fields, following a simplification of Ziberna et al. (2013) thermodynamic model. The iso-density line for $\rho = 3.40$ g/cm^3 is shown for reference.

Figure 3. Density profiles for fertile (left panel) and depleted (right panel) peridotitic systems calculated along a 45 mWm^{-2} geotherm. Brown to yellow colour bar represents the density variations along the profiles. Grey lines subdivide the ideal mantle sections into the spinel, spinel + garnet and garnet stability fields, following a simplification of Ziberna et al. (2013) thermodynamic model. The iso-density line for $\rho = 3.40$ g/cm^3 is shown for reference.

Figure 4. Density profiles for fertile (left panel) and depleted (right panel) peridotitic systems calculated along a 60 mWm^{-2} geotherm. Brown to yellow colour bar represents the density variations along the profiles. Grey lines subdivide the ideal mantle sections into the spinel, spinel + garnet and garnet stability fields, following a simplification of Ziberna et al. (2013) thermodynamic model. The iso-density line for $\rho = 3.40$ g/cm^3 is shown for reference.

Figure 5. Comparison of density profiles for fertile (left panel) and depleted (right panel) peridotitic systems calculated along a 35 mWm^{-2} geotherm (blue curves), 45 mWm^{-2} geotherm (yellow curves) and 60 mWm^{-2} geotherm (red curves). Density curves from previous literature are also shown: av. Lh (70 mWm^{-2}), av. Lh (50 mWm^{-2}), av. Hz (70 mWm^{-2}) and av. Hz (50 mWm^{-2}) are respectively the average density curves for fertile (TM16, BN4) and depleted (LS1, PA3) mantle xenoliths from Ziberna and Klemme (2016) calculated along the 70 mWm^{-2} and 50 mWm^{-2} geothermal gradients, whereas Inv. Lh (60-70 mWm^{-2}) and Inv. Hz (60-70 mWm^{-2}) are respectively the density curves of Inver lherzolite and harzburgite mantle xenoliths from Fullea et al. (2014) calculated under the Irish thermal state (60 to 70 mWm^{-2}).

Figure 6. Density profiles for PA3 (spinel harzburgite) and BN4 (spinel-garnet lherzolite) mantle xenoliths calculated along the 50 and 70 mWm^{-2} geothermal gradients following our simplified parameterisation in comparison with Perple_X-based original curves from Ziberna and Klemme (2016). Note the similarities between the two distinct sets of curves, both in their general trends and absolute values, as the density difference is always < 20 kg/m^3.

Figure 1

Click here to access/download;Figure;Figure 1.jpg

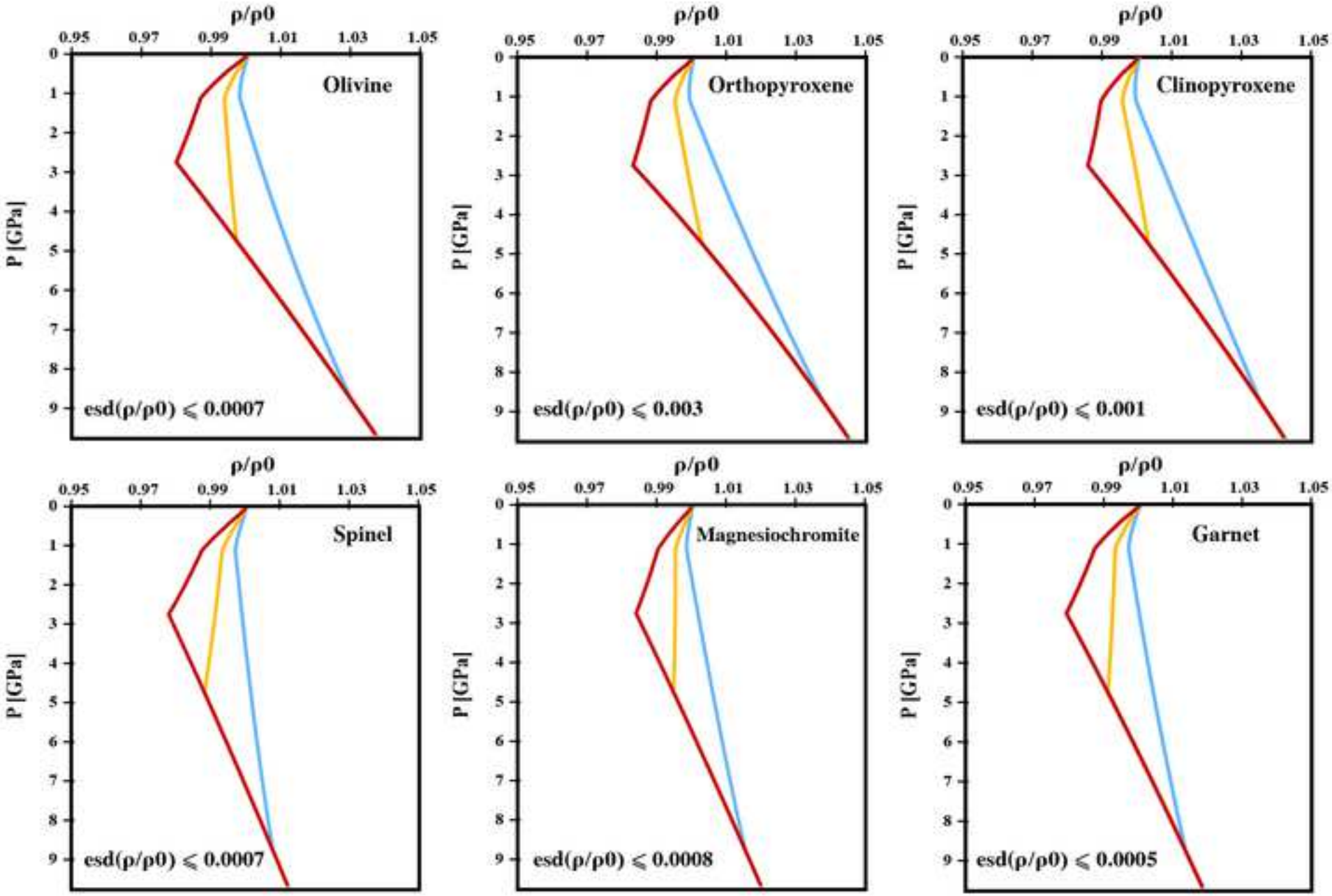

Figure 2

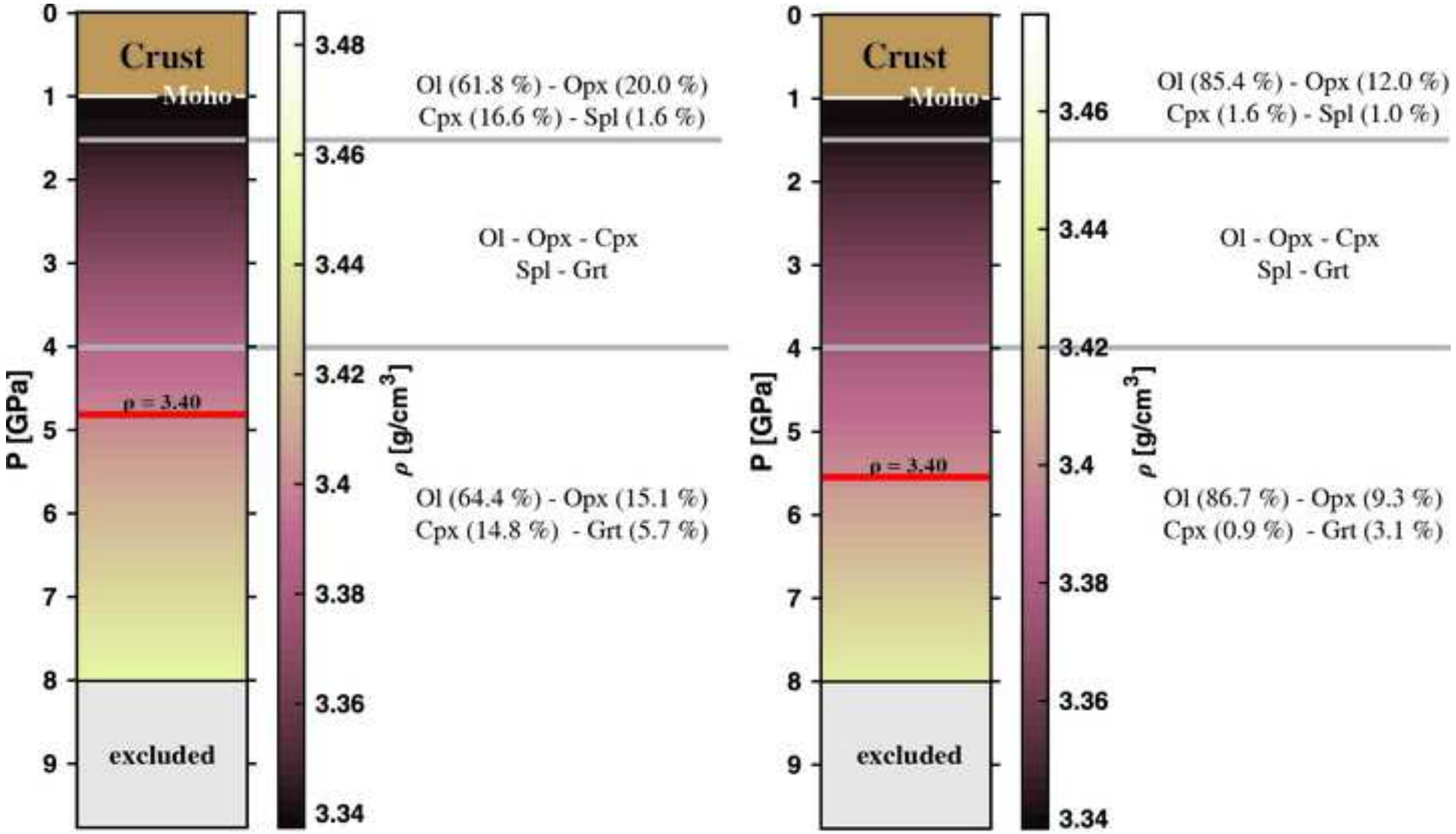

Figure 3

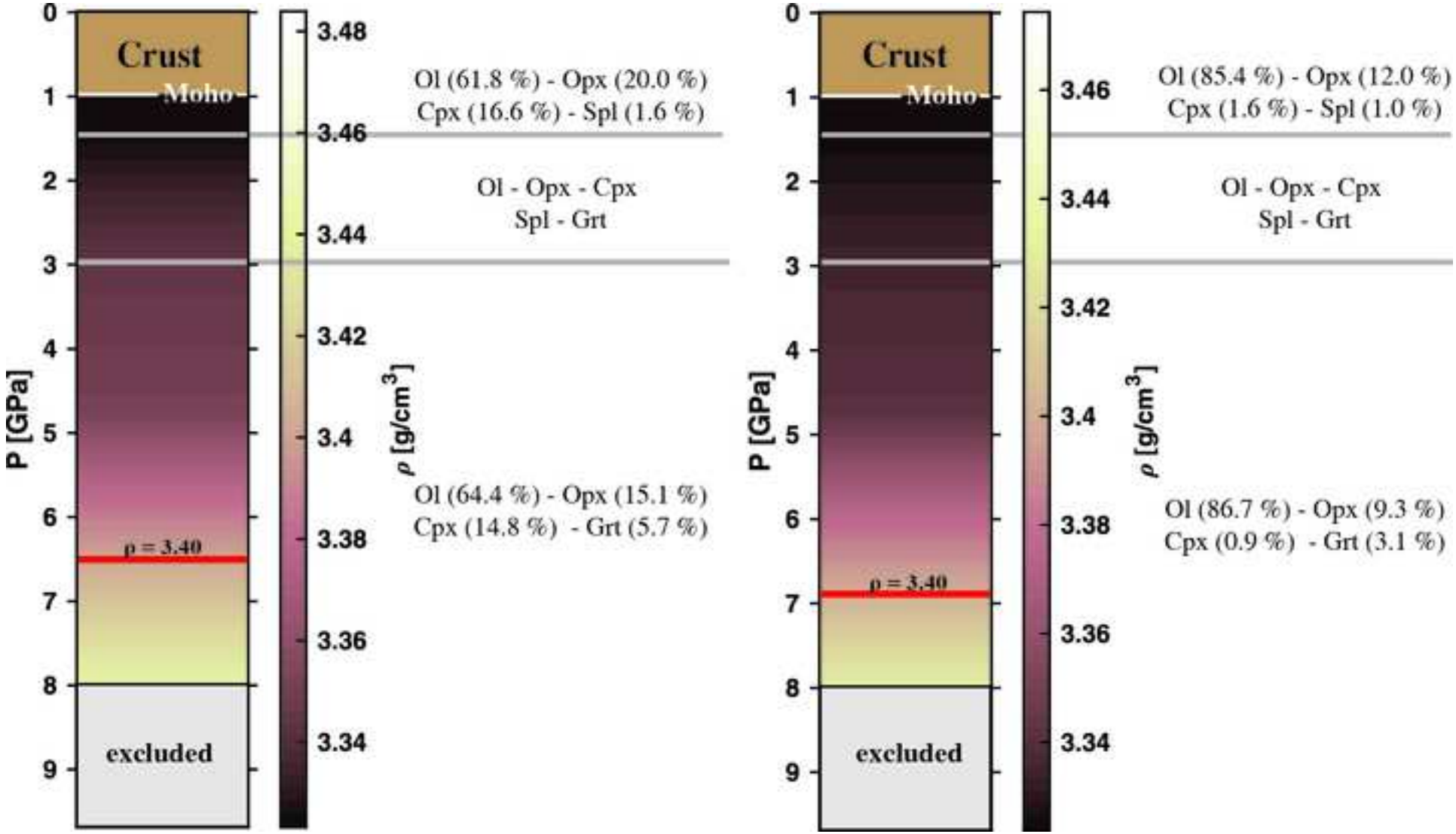

Figure 4

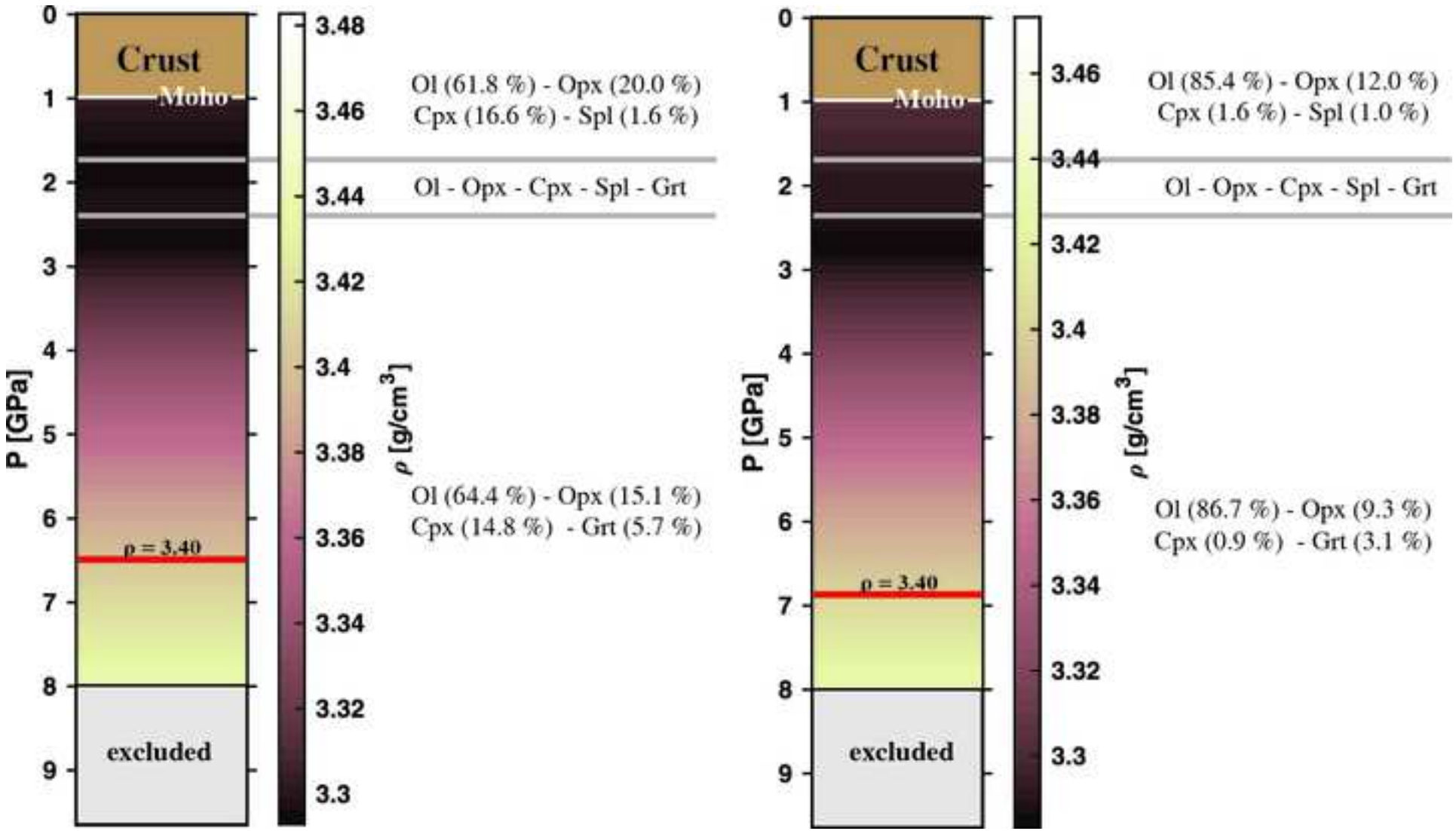

Figure 5

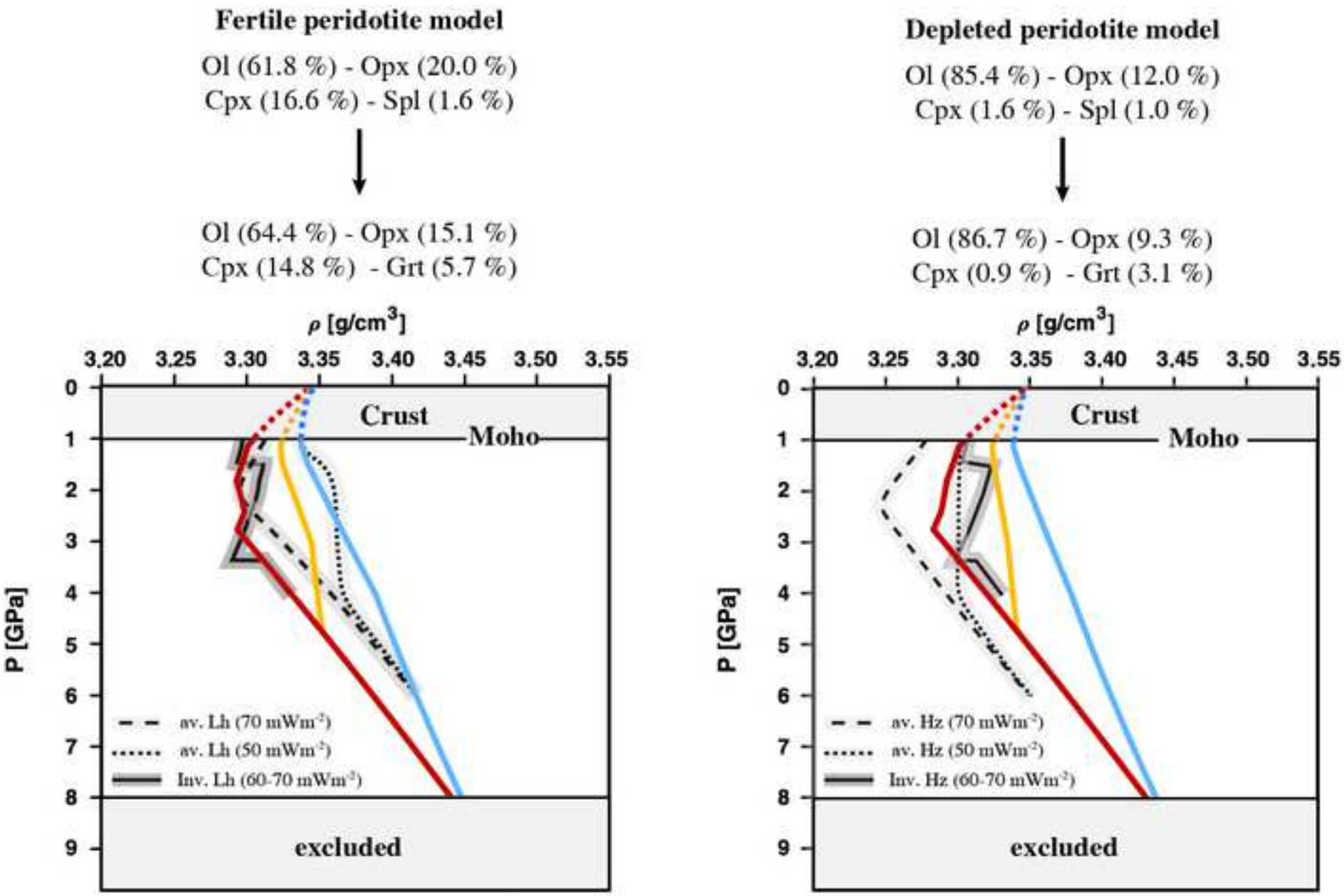

Figure 6

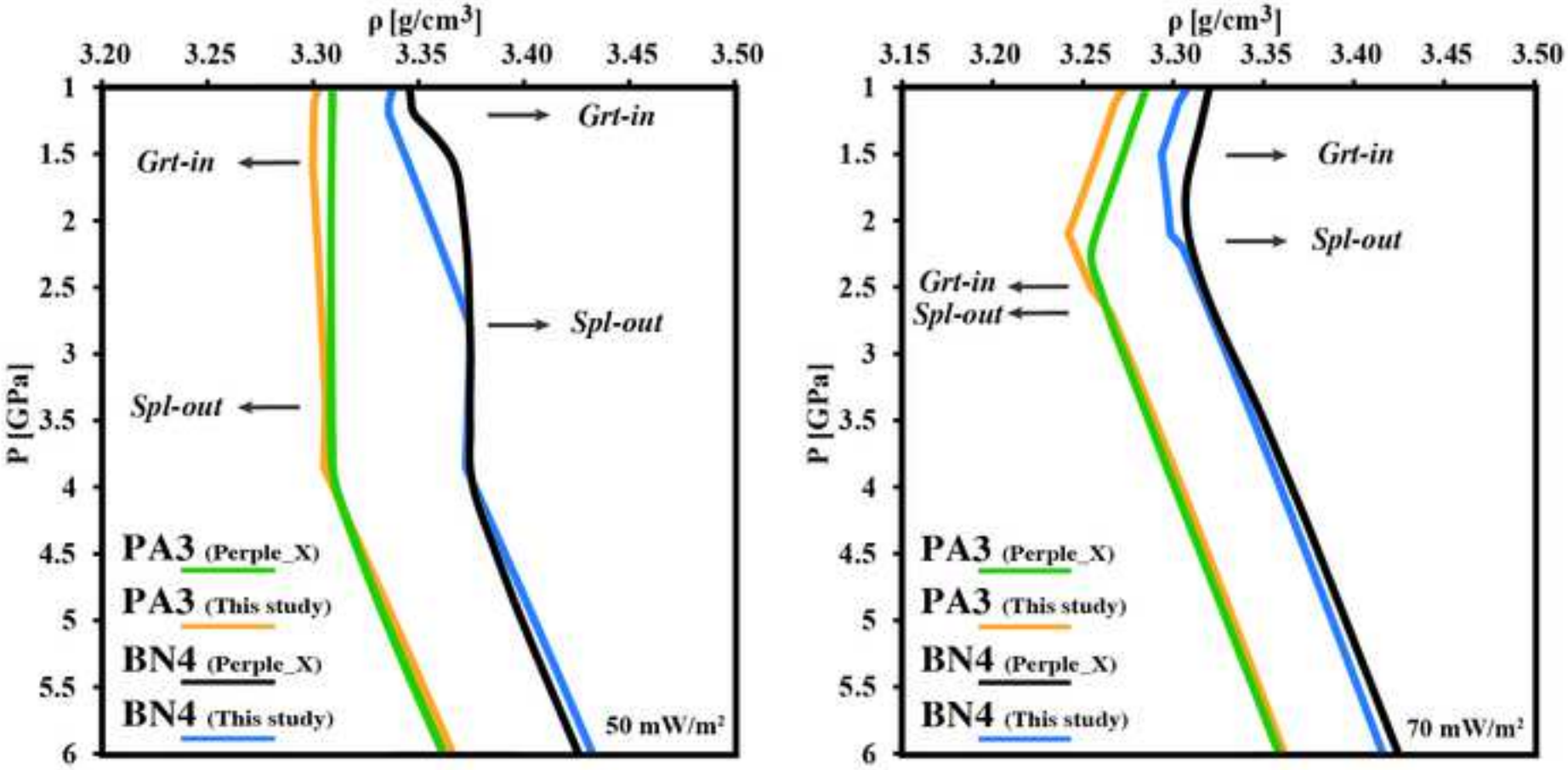

Table 1. Thermoelastic parameters selected from literature ([1] Angel et al., 2018; [2] Nestola et al., 2019) and derived from the fitting of P–V–T–K data for mantle phases. BM3 – Isothermal = Third-order Birch-Murnaghan compressional EoS in combination with the isothermal-type model (parameterisation from Angel et al., 2018); BM3 – HP = Third-order Birch-Murnaghan compressional EoS in combination with the Holland-Powell thermal‑pressure EoS; BM2 – HP = Second-order Birch-Murnaghan compressional EoS in combination with the Holland-Powell thermal‑pressure EoS.

	Olivine [1]	Orthopyroxene	Clinopyroxene	Spinel	Magnesiochromite [2]	Garnet
	BM3 – Isothermal	*BM3 – Isothermal*	*BM3 – Isothermal*	*BM3 – HP*	*BM2 – HP*	*BM3 – HP*
$K_{TR,0}$ (GPa)	126.4(2)	111.8(7)	112.8(3)	194.8(2)	183.3(5)	168.63(20)
$K'_{TR,0}$	4.51(5)	7.39(19)	4.95(9)	4.64(7)	4 *fixed*	5.11(9)
$K''_{TR,0}$	-0.0368 *implied*	-0.1681 *implied*	-0.0509 *implied*	-0.0254 *implied*	-0.0212 *implied*	-0.0369 *implied*
α_{V0} (K^{-1})	2.666(9) x 10^{-5}	2.591(18) x 10^{-5}	2.67(7) x 10^{-5}	1.86(2) x 10^{-5}	1.66(2) x 10^{-5}	2.392(9) x 10^{-5}
θ_E (K)	484(6)	510 *fixed*	343(58)	714(15)	683(16)	450(6)
δ_T	5.77(7)	9.0(6)	4.84(17)	-	-	-
δ'	-3.5(1.1)	0 *fixed*	0 *fixed*	-	-	-
γ_0	1.044 *fixed*	0.85 *fixed*	0.867 *fixed*	1.17 *fixed*	-	1.19 *fixed*
q	1.88 *fixed*	0 *fixed*	0 *fixed*	0 *fixed*	-	0 *fixed*
χ^2	*not reported*	0.94	0.44	0.93	1.1	1.51
N data	121	73	74	93	53	85

Table 2. Mineral phases compositions (a.p.f.u.) and modes (SG34 spinel lherzolite) and selected reference phases for the computation of density profiles for the fertile lithospheric mantle section. References: [1] Zha et al., 1998; [2] Chai et al., 1997, [3] Brown and Collins, 1998; [4] Ono et al., 2018; [5] Sumino and Nishizawa, 1978 (PY-1 sample); [#] = esd assumed, Fe* = total iron, n.d. = not detected, n.a. = not available.

	Olivine		**Orthopyroxene**		**Clinopyroxene**		**Spinel**		**Garnet**	
	Model	Selected [1]	Model	Selected [2]	Model	Selected [3]	Model	Selected [4]	Model	Selected [5]
Si	0.9955	1.00	1.8690	1.89	1.8570	1.8756	n.d.	n.d.	n.a.	3.0005
Ti	n.d.	n.d.	0.0029	n.d.	0.0136	0.0129	0.0016	0.0031	n.a.	0.0272
Al	n.d.	n.d.	0.2225	0.23	0.3437	0.2833	1.7484	1.7673	n.a.	1.7749
Cr	n.d.	n.d.	0.0115	0.01	0.0256	0.0275	0.1734	0.1871	n.a.	0.1202
Fe*	0.2106	0.20	0.2046	0.17	0.0983	0.0907	0.2761	0.2237	n.a.	0.5317
Mn	0.0017	n.d.	0.0035	0.01	0.0031	0.0026	0.0020	0.0020	n.a.	0.0217
Mg	1.7882	1.80	1.6745	1.63	0.7705	0.8513	0.7915	0.8090	n.a.	2.1868
Ca	0.0005	n.d.	0.0201	0.04	0.7782	0.7596	n.d.	n.d.	n.a.	0.3326
Na	n.d.	n.d.	n.d.	n.d.	0.1097	0.1050	n.d.	n.d.	n.a.	n.d.
K	n.d.	n.d.	n.d.	n.d.	n.d.	n.d.	n.d.	n.d.	n.a.	n.d.
Ni	0.0079	n.d.	0.0025	n.d.	n.d.	0.0001	0.0070	0.0079	n.a.	n.d.
Zn	n.d.	n.d.	n.d.	n.d.	n.d.	n.d.	0.0035	n.d.	n.a.	n.d.
Unit cell volume [Å^3]	n.a.	292.01(10)	n.a.	834.1(5)[#]	n.a.	432.96(4)	n.a.	538.78(6)	-	1535.2(5)[#]
Mode [spl stability field]	61.8		20.0		16.6		1.6		0.0	
Mode [grt stability field]	64.4		15.1		14.8		0.0		5.7	

Table 3. Mineral phases compositions (a.p.f.u.) and modes (NDR13 spinel harzburgite) and selected reference phases for the computation of density profiles for the depleted lithospheric mantle section. References: [1] Zha et al., 1998; [2] Gatta et al., 2007; [3] Comodi et al., 1995 (sample 3211); [4] Matsukage et al., 2010; [5] Babuška et al., 1978 (PY-2 sample); Fe* = total iron, n.d. = not detected, n.a. = not available.

	Olivine		**Orthopyroxene**		**Clinopyroxene**		**Magnesiochromite**		**Garnet**	
	Model	Selected [1]	Model	Selected [2]	Model	Selected [3]	Model	Selected [4]	Model	Selected [5]
Si	1.0031	1.00	1.9687	1.968	1.9568	1.962	0.0004	n.d.	n.a.	3.0105
Ti	n.d.	n.d.	0.0005	n.d.	0.0021	0.002	0.0017	n.d.	n.a.	0.0160
Al	0.0004	n.d.	0.0545	0.037	0.0753	0.121	0.7961	1.00	n.a.	1.7297
Cr	0.0005	n.d.	0.0142	0.011	0.0494	0.023	1.1240	0.92	n.a.	0.1780
Fe*	0.1851	0.20	0.1682	0.146	0.0816	0.072	0.3618	0.31	n.a.	0.4874
Mn	0.0028	n.d.	0.0044	n.d.	0.0029	0.001	0.0019	n.d.	n.a.	0.0198
Mg	1.7965	1.80	1.7454	1.813	0.9779	0.890	0.7057	0.77	n.a.	2.1910
Ca	0.0012	n.d.	0.0344	0.025	0.7985	0.828	0.0003	n.d.	n.a.	0.3575
Na	n.d.	n.d.	0.0071	n.d.	0.0642	0.102	n.d.	n.d.	n.a.	n.d.
K	n.d.	n.d.	n.d.	n.d.	0.0004	n.d	n.d.	n.d.	n.a.	n.d.
Ni	0.0070	n.d.	0.0025	n.d.	0.0019	n.d	0.0045	n.d.	n.a.	n.d.
Zn	n.d.	n.d.	n.d.	n.d.	n.d.	n.d	0.0035	n.d.	n.a.	n.d.
Unit cell volume [Å^3]	n.a.	292.01(10)	n.a.	834.71(3)	n.a.	434.42(48)	n.a.	560.68(16)	-	1537.20(46)
Mode [spl stability field]	85.4		12.0		1.6		1.0		0.0	
Mode [grt stability field]	86.7		9.3		0.9		0.0		3.1	

Declaration of interests

☒ The authors declare that they have no known competing financial interests or personal relationships that could have appeared to influence the work reported in this paper.

☐The authors declare the following financial interests/personal relationships which may be considered as potential competing interests:
